Direct in-situ Estimates of Energy and Force Balance in Near Earth Collisionless Plasmas

Souhail Dahani (1), Benoit Lavraud (1, 2), Vincent Génot (1), Sergio Toledo-Redondo (3), Rungployphan Kieokaew (1), Naïs Fargette (4), Owen W. Roberts (5), Daniel Gershman (6), Yoshifumi Saito (7), Barbara Giles (6), Roy Torbert (8) and James Burch (9)

(1) Institut de Recherche en Astrophysique et Planétologie, CNRS, UPS, CNES, Université de Toulouse, Toulouse, France
(2) Laboratoire d'Astrophysique de Bordeaux, CNRS, University of Bordeaux, Pessac, France
(3) Department of Electromagnetism and Electronics, University of Murcia, Murcia, Spain
(4) The Blackett Laboratory, Imperial College London, London, United Kingdom
(5) Space Research Institute, Austrian Academy of Sciences, Graz, Austria
(6) NASA Goddard Space Flight Center, Greenbelt, MD, USA
(7) Institute of Space and Astronautical Science, JAXA, Sagamihara, Japan,
(8) Space Science Center, University of New Hampshire, Durham, NH, USA
(9) Southwest Research Institute, San Antonio, TX, USA

Corresponding author: Souhail Dahani (sdahani@irap.omp.eu)

Key Points:

- We analyze energy and force balance in the monofluid and multifluid frameworks using MMS data
- We show that MMS is able to capture energy and force balance in the monofluid and ion fluid frameworks
- The ratio of spacecraft separation to local gradient scale limits the proper estimation of electron pressure gradient terms

Abstract

Fundamental processes in plasmas act to convert energies into different forms, e.g., electromagnetic, kinetic and thermal. Direct derivation from the Valsov-Maxwell equation yields sets of equations that describe the temporal evolution of the magnetic, kinetic and internal energies in either the monofluid or multifluid frameworks. In this work we focus on the main terms that affect the changes in the kinetic energy. These are pressure gradient-related terms and electromagnetic terms. The former account for plasma acceleration or deceleration from a pressure gradient, while the latter from an electric field. The overall balance between these terms is fundamental to ensure the conservation of energy and momentum. We use in-situ observations from the Magnetospheric MultiScale (MMS) mission to study the relationship between these terms. We perform a statistical analysis of those parameters in the context of magnetic reconnection by focusing on small-scale Electron Diffusion Regions and large-scale Flux Transfer Events. The analysis reveals a correlation between the two terms in the monofluid force balance, and in the ion force and energy balance. However, the expected relationship cannot be verified from electron measurements. Generally, the pressure gradient related terms are smaller than their electromagnetic counterparts. We perform an error analysis to quantify the expected underestimation of gradient values as a function of the spacecraft separation compared to the gradient scale. Our findings highlight that MMS is capable of capturing energy and force balance for the ion fluid, but that care should be taken for energy conversion terms based on electron pressure gradients.

1. Introduction

Energy conversion processes in collisionless space plasmas are triggered by various complex mechanisms involved in the overall plasma dynamics. Magnetic reconnection is one of these fundamental mechanisms during which the magnetic field lines break and reconnect, and is accompanied with such energy conversions. Magnetic reconnection transfers magnetic to kinetic and thermal energies in key regions in which particles decouple from the magnetic field, breaking the frozen-in law. Ions decouple from the magnetic field in a region scaling on the order of ion inertial lengths, and called the ion diffusion region (IDR), while electrons decouple in a much smaller region of the order of few electron inertial lengths, and called the electron diffusion region (EDR). On a larger scale, magnetic reconnection has a strong impact on the global dynamics of the magnetosphere, and on the overall topology of the magnetopause. In particular, the sequential occurrence of magnetic reconnection at the dayside magnetopause is responsible for the creation of Flux Transfer Events (FTEs). FTEs are observed on the dayside magnetopause, at Earth and at other planets (like Mercury; Slavin et al., 2012). They are magnetic flux ropes that form a helicoidal magnetic topology in between two consecutive magnetic reconnection X-line (e.g., Hasegawa et al., 2010; Øieroset et al., 2011; Raeder et al., 2006).

Energy conversion associated with magnetic reconnection involves exchanges between energy forms, i.e., electromagnetic, kinetic and thermal energies. The terms that quantify the energy exchanges between these forms are present in the monofluid and multifluid energy equations that we detail in the next section. In analyses related to magnetic reconnection, the term $\vec{J} \cdot \vec{E}'$ (Zenitani et al., 2011) is commonly employed

as a measure of energy dissipation, although it is actually representing energy conversion from magnetic energy to thermal (or internal) energy (e.g., Burch et al., 2016.; Genestreti et al., 2018). Another term that recently gained prominence as a measure of dissipation is the pressure strain term ($-(\bar{\bar{P}} \cdot \vec{\nabla}) \cdot \vec{v}$; Yang et al., 2017). It quantifies plasma cooling or heating along with its incompressive decomposition ($\Pi_{ij} D_{ij}$). This term has been measured in magnetic reconnection (e.g., Bandyopadhyay et al., 2021), in EDRs (e.g., Zhou et al., 2021), in the turbulent magnetosheath (e.g., Wang et al., 2021) and in dipolarization fronts (e.g., Zhong et al., 2019). In addition to examining terms that influence thermal energy, it is crucial to study the effects on kinetic energy in the context of magnetic reconnection. The present study particularly focuses on the terms that affect the kinetic energy and their balance.

Fadanelli et al. (2021) recently examined energy conversion terms associated with magnetic reconnection using a multifluid approach. In their work, they focused on a magnetic reconnection site within turbulent plasma using a hybrid-Vlasov code. They analyzed the source terms (which we will explain in more detail in the next section) responsible for changing both kinetic and internal (or thermal) energies. Their findings show that there is an almost perfect linear relationship between the source terms responsible for kinetic energy variation, suggesting that, in this set-up, these source terms tend to balance each other at all times, to first order. It is expected that these terms are large in absolute value, and that it is their difference that accounts for bulk plasma acceleration, i.e., leading to an actual change in the time derivative of kinetic energy. Their results are in accordance with theoretical expectations as well as other works with different simulation approaches (e.g., Agudelo Rueda et al., 2022). The particularity of the work by Fadanelli et al. (2021) is the measure of the energy terms in a point-by-point basis at the reconnection site and its close environment in the simulation domain instead of integrating the terms over the whole simulation domain (in which case the boundary conditions have a strong impact on the results). Another advantage of the point-by-point approach is that it offers a more straightforward way of comparison with spacecraft observation.

To our knowledge, there is yet no study that has attempted to assess kinetic energy balance in space plasmas based on in situ spacecraft data. However, several works focussed on EDRs (e.g., Torbert et al., 2016, 2017) and dipolarization fronts (e.g., Yao et al., 2017; Alqeeq et al., 2022) study the Ohm's law to determine and compare the measured electric field in the electron frame with the electric field that results from the action of the electron pressure gradient. Such analysis involves an indirect energy and force balance test of the electron fluid and notably the force balance in the multifluid framework as will be apparent in the next section.

In the present study, we examine statistically the force and kinetic energy balance using in-situ data from Magnetospheric MultiScale (MMS) mission in the context of EDRs and FTEs observations, which are ideal events to study the energy conversion associated with the magnetic reconnection process. The outline of this paper is as follows. Section 2 presents the theoretical context related to this work where we detail the

energy and force terms. Section 3 presents data from the MMS mission and the methodology for interval determination and terms measurements. Section 4 presents example analyses for an EDR and for an FTE. Sections 5, 6 and 7 present our findings on monofluid force balance, multifluid force balance and multifluid kinetic energy balance, respectively, with case and statistical studies. Finally, section 8 presents discussions and conclusions.

2. Theoretical context

The theoretical framework underlying this study is based on the momentum and energy equations derived directly from the Vlasov equation. Our investigation examines plasma behavior within both monofluid and multifluid frameworks, building upon previous work such as that of Birn & Hesse (2010) and Fadanelli et al. (2021). In a monofluid description, the equation for the conservation of momentum is given as:

$$\partial_t(\rho\vec{v}) + \vec{\nabla}\cdot(\rho\vec{v}\vec{v}) = \vec{J}\times\vec{B} - \vec{\nabla}\cdot\bar{\bar{P}}$$

where ρ is the mass density, $\vec{v}$ is the bulk velocity, $\vec{J}$ the total current density, $\bar{\bar{P}}$ the pressure tensor and $\vec{B}$ is the magnetic field. The right-hand side of the equation depicts forces acting on the plasma, namely the Lorentz force and the pressure gradient force.

In both monofluid and multifluid scenarios, force balance is crucial for momentum conservation. This balance, represented by $\vec{J}\times\vec{B} = \vec{\nabla}\cdot\bar{\bar{P}}$ in the monofluid case, extends to $q_s n_s(\vec{E} + \vec{v}_s\times\vec{B}) = \vec{\nabla}\cdot\bar{\bar{P}}_s$ in the multifluid case, where $s = \{e, i\}$ denotes the particle species with "e" for electrons and "i" for ions. q_s, n_s, $\vec{v}_s$ and $\bar{\bar{P}}_s$ represent the charge, number density, velocity vector and pressure tensor for the species "s", respectively. $\vec{E}$ is the electric field.

The multifluid framework also includes an equation describing the evolution of the kinetic energy density, as formulated by Fadanelli et al. (2021):

$$d_t K_s = (\partial_t + \vec{v}_s\cdot\vec{\nabla})K_s = -K_s\vec{\nabla}\cdot\vec{v}_s - \vec{v}_s\cdot\vec{\nabla}\cdot\bar{\bar{P}}_s + \vec{j}_s\cdot\vec{E}$$

where $K_s = 1/2 m_s n_s \vec{v}_s^2$ is the kinetic energy density with m_s is the species mass, $\vec{j}_s = q_s n_s \vec{v}_s$ is the species "s" current density. The left hand side of the equation represents the Lagrangian derivative quantifying the rate of change of the kinetic energy density at a moving point (Lagrangian viewpoint), the derivative includes the rate of change at a fixed point (∂_t; Euler viewpoint) and the advection term ($\vec{v}_s\cdot\vec{\nabla}$). The right-hand side of the equation represents the terms responsible for kinetic energy density variations. There are source terms, i.e., $\vec{j}_s\cdot\vec{E}$ and $-\vec{v}_s\cdot\vec{\nabla}\cdot\bar{\bar{P}}_s$ and non-source terms, i.e., $-K_s\vec{\nabla}\cdot\vec{v}_s$. We discuss below the details of each term in the right-hand side of the equation.

The term $\vec{j}_s \cdot \vec{E}$ accounts for plasma acceleration or deceleration due to an electric field in this context (kinetic energy equation). This term is also present in the Poynting theorem as a source term for generation or dissipation of magnetic energy. Hence, it provides a link between magnetic energy and kinetic energy. In the monofluid version, the two terms equivalent to $\vec{j}_s \cdot \vec{E}$ are $\vec{J} \cdot \vec{E}'$ and $\vec{v} \cdot (\vec{J} \times \vec{B})$. The Joule dissipation ($\vec{J} \cdot \vec{E}'$; Zenitani et al., 2011; Birn & Hesse 2010) is found in the monofluid version of the Poynting theorem and in the thermal (or internal) energy density equation. It quantifies the direct energy exchanges between magnetic energy and thermal energy. As presented earlier, in the multifluid version, this measure requires passage through the kinetic energy equation, and then to thermal energy through the balance with the pressure term. The fluid term that measures energy transfer from magnetic energy to kinetic energy is $\vec{v} \cdot (\vec{J} \times \vec{B})$. It is obtained by multiplying the momentum equation with the bulk velocity; this term describes plasma acceleration or deceleration due to the Lorentz force action on the plasma.

The term $-\vec{v}_s \cdot \vec{\nabla} \cdot \bar{\bar{P}}_s$ accounts for plasma acceleration or deceleration due to a pressure gradient. This term is particularly interesting because it links kinetic energy to thermal energy. This link depends on the general framework in which we measure. For instance, the transfer between kinetic energy and thermal energy is directly observed in a closed and periodic system, e.g., in a simulation framework, which makes it mathematically convenient to neglect divergence terms through integration of the energy equations to get overall energy budgets. In this case, the divergence of the work of the mechanical stress, i.e., $\vec{\nabla} \cdot (\bar{\bar{P}} \cdot \vec{v})$ vanishes. It decomposes into the pressure gradient term and the pressure strain term (Yang et al., 2017), i.e., $\vec{\nabla} \cdot (\bar{\bar{P}} \cdot \vec{v}) = \vec{v} \cdot \vec{\nabla} \cdot \bar{\bar{P}} + (\bar{\bar{P}} \cdot \vec{\nabla}) \cdot \vec{v}$, which then are similar. They measure energy transfers between kinetic and thermal energies. However, in a more general framework, e.g., real observations, such direct link is not obvious as one should take into account the divergence of the work of the mechanical stress ($\vec{\nabla} \cdot (\bar{\bar{P}} \cdot \vec{v})$). In this case we consider separately the pressure term ($-\vec{v} \cdot \vec{\nabla} \cdot \bar{\bar{P}}$) and the pressure strain term ($-(\bar{\bar{P}} \cdot \vec{\nabla}) \cdot \vec{v}$) so we can assess thermodynamic work contribution in acceleration separately from its contribution in plasma heating.

The term $-K_s \vec{\nabla} \cdot \vec{v}_s$ describes the expansion or compression (a visualization could be found in Figure 1 of Del Sarto & Pegoraro, 2018) of the plasma fluid and how it changes the kinetic energy density spatially. The term $-K_s \vec{\nabla} \cdot \vec{v}_s$ does not contribute to the kinetic energy density as a source term but it contributes to the general rate of change in the kinetic energy density.

Reorganizing terms within this equation yields another representation, implying conservation of kinetic energy and highlighting kinetic energy source terms:

$$\partial_t K_s + \vec{\nabla} \cdot (K_s \vec{v}_s) = -\vec{v}_s \cdot \vec{\nabla} \cdot \bar{\bar{P}}_s + \vec{j}_s \cdot \vec{E}$$

The conservation of kinetic energy density implies that the terms in the RHS cancel each others, i.e., $\vec{v}_s \cdot \vec{\nabla} \cdot \bar{\bar{P}}_s = \vec{j}_s \cdot \vec{E}$.

In this work, we test force balance in both the monofluid and multifluid frameworks, as well as the energy balance in the multifluid framework. This is accomplished by statistically measuring the correlations between these various terms in different plasma environments, i.e., Electron Diffusion Regions and Flux Transfer Events.

3. Data and Methods

We utilize burst mode data from the MMS (Burch et al., 2016) mission in the Geocentric Solar Ecliptic (GSE) coordinate system. We use magnetic field measurements from the FluxGate Magnetometer (FGM; Russell et al., 2016) at 0.01 s resolution. We use electric field measurements from the Electric Field Double Probes (EDP; Ergun et al., 2016; Lindqvist et al., 2016) at 15 µs resolution. We use plasma moments, i.e., number density, bulk velocity, temperature and pressure, from the Fast Plasma Investigation (FPI; Pollock et al., 2016) at 30 ms resolution for electrons (FPI-DES) and 150 ms for ions (FPI-DIS).

We make use of an EDR list compiled by Webster et al. (2018) including individual EDRs selected from the literature (references therein) and new candidates based on visual inspection of EDR signatures, e.g., electron agyrotropy, positive $\vec{J} \cdot \vec{E}'$ and crescent shaped velocity distribution functions. We supplement this list with a second list compiled in Lenouvel et al. (2021) and Lenouvel (2022) which rely on machine learning techniques for EDR signatures detection. A full list aggregating these three references can be found in the Zenodo dataset, Lenouvel et al. (2023). The FTE events we use in this study are a sublist of a list compiled by Fargette et al. (2020) based on visual inspection of FTE signatures, e.g., bipolar variation in the normal component of the magnetic field to the unperturbed magnetopause (Rijnbeek et al., 1982; Russell & Elphic, 1978) and an enhancement of the total magnetic field (Paschmann et al., 1982). This list can be found in the supplementary information of Kieokaew et al. (2021).

The choice of the interval duration for every event is not straightforward. The FTE list consists of intervals marked by the start and the end of the bipolar variation accompanied with the enhancement in the total magnetic field. By contrast, intervals around EDRs are more tricky to choose as the EDRs are generally represented by a single time, i.e., the EDR time encounter. We tested several interval durations around the EDR and chose 4 s intervals, in which we maximize the correlation coefficient, as will be described in the following sections.

We apply multi-spacecraft techniques (Paschmann & Daly, 1998) to evaluate the gradient terms. We average the electric field to ion and electron moments resolution, to measure $\vec{j}_s \cdot \vec{E}$, respectively, which in

turn is averaged over the 4 spacecraft. We average electron moments, the electric field and the magnetic field to ion moments resolution to evaluate the fluid terms, i.e.,$\vec{J} \cdot \vec{E}'$, $\vec{J} \times \vec{B}$ and $\vec{\nabla} \cdot \bar{\bar{P}}$. Similarly, $\vec{v}_s$, $\vec{J} \cdot \vec{E}'$ and $\vec{J} \times \vec{B}$ are averaged over the 4 spacecraft.

Although the equation and general balance in conversion terms does not depend on the reference frame, the actual values of the main terms in the multifluid kinetic energy equation are frame dependent, i.e., $\vec{j}_s \cdot \vec{E}$ *and* $\vec{v}_s \cdot \vec{\nabla} \cdot \bar{\bar{P}}_s$. Hence, for our purposes it is best to find a suitable reference frame. We choose to measure these terms in the local moving frame linked to the event (EDR frame or FTE frame), therefore, determining their proper velocities filtered out from the surrounding plasma is essential. In this work we opt for a simple and obvious reference frame, as in Eastwood et al. (2020), that consists in linking the structure velocity with the background plasma flow velocity if we assume a uniform steady structure motion. We apply the following transformations: $\vec{v}_s \rightarrow \vec{v}_s - \vec{v}_{event}$ and $\vec{E} \rightarrow \vec{E} + \vec{v}_{event} \times \vec{B}$, where $\vec{v}_{event}$ is the event velocity. For EDRs $\vec{v}_{event}$ taken to be the ion velocity averaged over three points surrounding the EDR time taken from the published list, while for FTE events we take it to be the average ion velocity during the FTE interval.

4. Event illustration

In this section we introduce a case study for each type of event (EDR and FTE) as an illustration. In the next sections we will be focusing on statistical studies with a particular attention to these two case studies to complement our quantitative analyses and provide a context for the statistical findings.

Figure 1 shows an example of an EDR event observed by MMS4 on 2016-11-13 around 09:10:40.760 UT located at [8.94, 5.21, -0.47] Earth radii in Geocentric Solar Ecliptic (GSE) coordinates, highlighted by the red dashed line across the panels. The EDR is observed close to the magnetopause boundary at around 09:10:40. The boundary is visible from the crossing from the magnetosphere to the magnetosheath as observed with the changes in plasma properties. The magnetosphere (magnetosheath) has low (high) density (panel (e)) and low (high) fluxes of low energy ions (panel (h)) and high (low) fluxes of high energy ions (panel (h)). We take the interval highlighted in gray shading across the panels as the interval related to this particular event as explained in the past section. We observe several key signatures related to EDRs at this time. Large electron jets (Khotyaintsev et al., 2016) are visible in all the components of the electron velocity with the higher value reaching about +1000 km/s in the z-component (panel (b)) indicating the spacecraft crossing northward through an ongoing magnetic reconnection site. A localized increase in the normal electric field (Norgren et al., 2016; Shay et al., 2016; Torbert et al., 2016; in panel (d)) is visible close to the X line; electron demagnetization (Burch et al., 2016), which is visible with a localized peak in the total electric field in electrons rest frame (black line; panel (f)), implying the departure from the ideal Ohm's law. A high increase in the Joule dissipation is shown by the peak in the $\vec{J} \cdot \vec{E}'$

quantity (Zenitani et al., 2011; in panel (g)); this term quantifies the direct energy transfer from magnetic energy to heat (Birn & Hesse, 2010), and is highly used as an indicator of magnetic reconnection. Another characteristic feature of EDRs is the crescent shaped velocity distribution function, also observed at this event (not shown here).

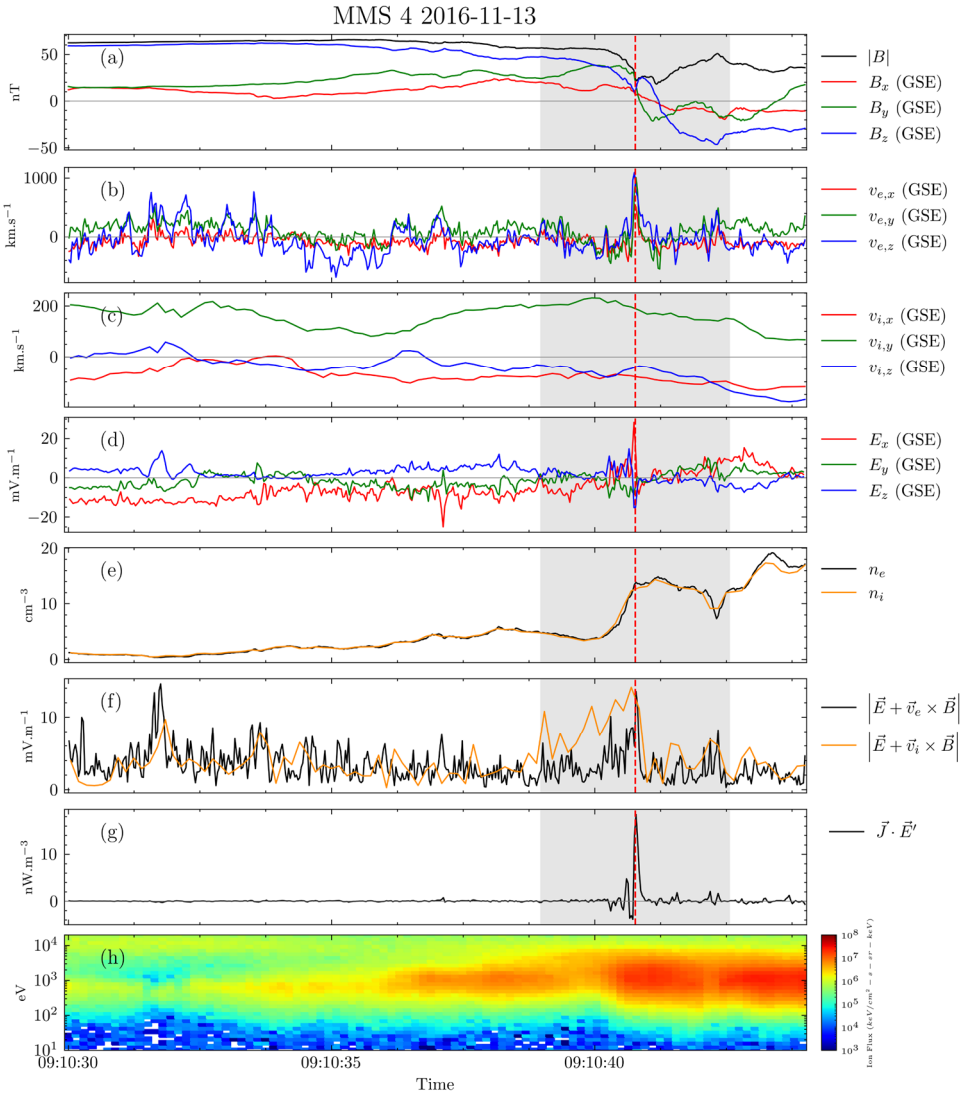

Figure 1: MMS 4 observations of an EDR found at 2016-11-13T09:10:40.760 UT highlighted by the red dashed line across panels (a) to (g). Panel (a) shows the magnetic field in the GSE coordinate system. Panels (b) and (c) show the electron and ion velocities, respectively, in the GSE coordinate system. Panel (d) shows the electric field in the GSE coordinate system. Panel (e) shows the electron (black) and ion (orange) number densities. Panel (f) shows the magnitude of the electric field in electrons (black) and ions (orange) rest frame. Panel (g) shows the Joule dissipation. Panel (h) shows the ion energy spectrogram. The gray shaded region shown across panels (a) to (g) marks the EDR interval used.

Figure 2 shows an example of an FTE event observed by MMS1 on 2015-11-05 between around 04:58:42 UT and 04:58:51 UT located at [10.46, 2.04, -0.47] Earth Radii in GSE coordinates, highlighted by the gray shading across the panels. FTEs main signature stands out from the surrounding environment. The bipolar variation (Rijnbeek et al., 1982; Russell & Elphic, 1978) is visible on the x-component of the magnetic field (panel (a)) that represents roughly the normal to the magnetopause, which is consistent

with a dayside event close to the subsolar point. A clear enhancement in the magnitude of the magnetic field (Paschmann et al., 1982; in panel (a)) is also observed during the bipolar variation. We include other plasma parameters for more context, e.g., electron and ion velocities in panel (b) and (c), respectively; the electric field in panel plasma number density in panel (d); ion temperatures parallel and perpendicular to the magnetic field in panel (e); ion energy spectrogram in panel (f).

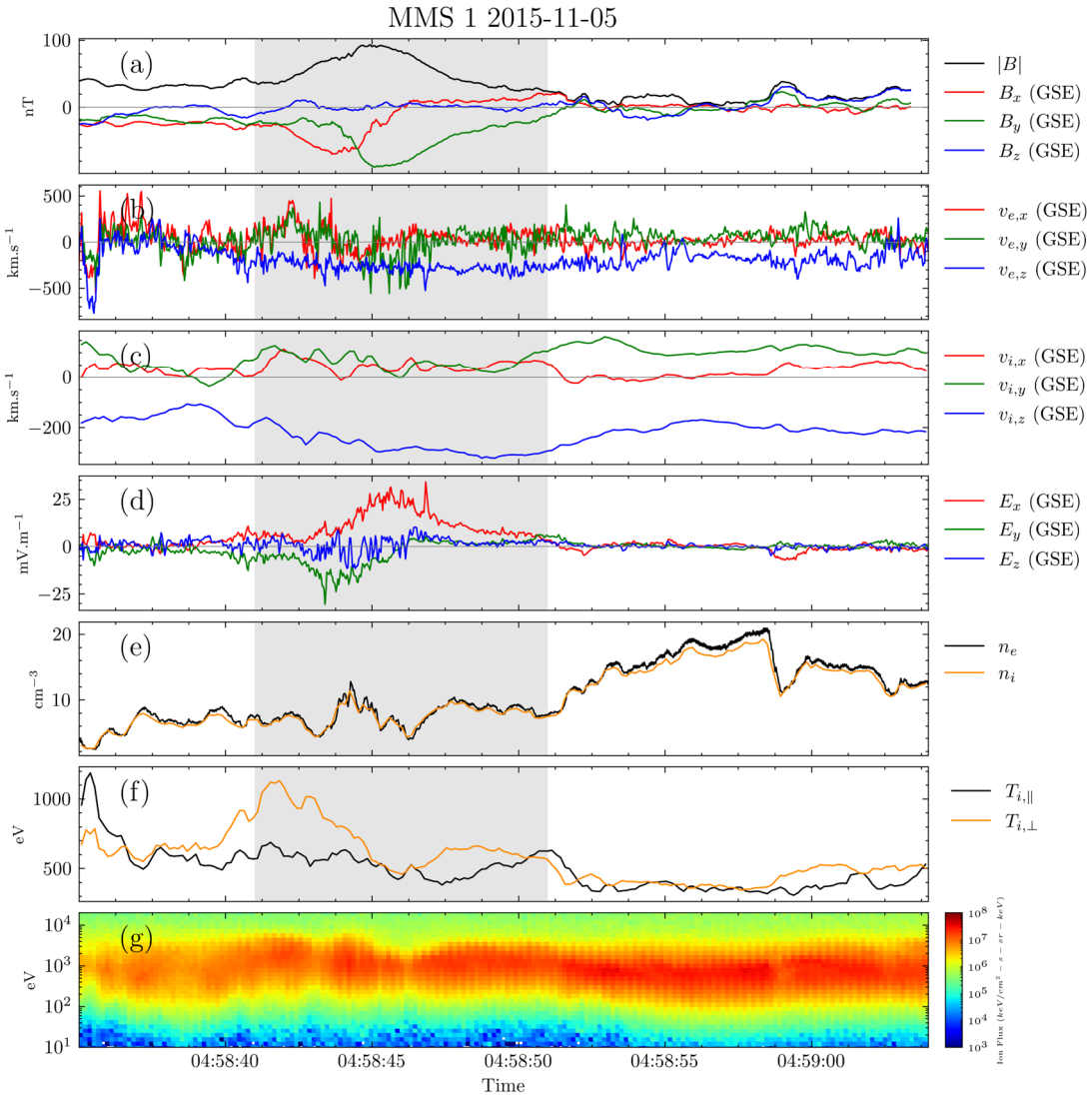

Figure 2: MMS 1 observations of an FTE on 2015-11-05 between 04:58:42 UT and 04:58:51 UT, highlighted with the gray shaded region as shown across the panels (a) to (f). Panel (a) shows the magnetic field in the GSE coordinate system. Panel (b) and (c) show electron and ion velocities, respectively, in the GSE coordinate system. Panel (d) shows the electric field in the GSE coordinate system. Panel (e) shows the electron (black) and ion (orange) number densities. Panel (f) shows ions parallel (black) and perpendicular (orange) temperature. Panel (g) shows the ions energy spectrogram.

5. Monofluid force balance

We focus in this section on the fluid terms describing the forces at work in the plasma as introduced in the momentum equation, including the Lorentz force, i.e., $\vec{J} \times \vec{B}$ and the pressure gradient force i.e., $\vec{\nabla} \cdot \bar{\bar{P}}$.

We first analyze two case studies, one for each type of event (EDR and FTE). We then provide statistical results.

5.1 Case studies

Figure 3 illustrates measurements of both $\vec{J} \times \vec{B}$ and $\vec{\nabla} \cdot \bar{\bar{P}}$ corresponding to the EDR event introduced in Figure 1, and the relationship between their components, respectively, through scatter plots of $(\vec{J} \times \vec{B})_\alpha$ and $(\vec{\nabla} \cdot \bar{\bar{P}})_\alpha$, with $\alpha = \{x,\ y,\ z\}$. We perform linear regressions, represented by the black lines in the scatter plots, while the red lines indicate perfect linearity, i.e., $\vec{J} \times \vec{B} = \vec{\nabla} \cdot \bar{\bar{P}}$. For each component, we provide the linear correlation measure and the slope resulting from the linear regression. The slope estimation serves as an indicator of the ratio between $\vec{J} \times \vec{B}$ and $\vec{\nabla} \cdot \bar{\bar{P}}$. Notably, the three directions closely align with the red line, with slope values of 0.93, 0.7, and 0.95 for the x-, y-, and z-directions, respectively.

These results imply a positive, linear relationship between the two terms, reflecting a good force balance. The observed force balance is somewhat stronger in the x-direction (correlation coefficient of 0.7; note that the x-direction represents roughly the direction normal to the magnetopause) compared to the y- and z-directions (correlation coefficients of 0.5 and 0.58, respectively). Overall, these findings suggest a satisfactory force balance in this specific event across all three directions.

Figure 4 presents the same measurements for the FTE event introduced in Figure 2. The slopes for the x-, y-, and z-directions are 0.26, 0.47, and 0.71, respectively. These results suggest a weaker, yet positive, linear relationship between $\vec{J} \times \vec{B}$ and $\vec{\nabla} \cdot \bar{\bar{P}}$ during the FTE interval. The force balance, as indicated by the slopes, exhibits a less distinct alignment with the red line, with correlation coefficients of 0.16, 0.32, and 0.71 for the x-, y-, and z-directions, respectively. While the force balance is less evident than in the EDR event, the findings still suggest a reasonable balance, especially along the z-direction, during the FTE event.

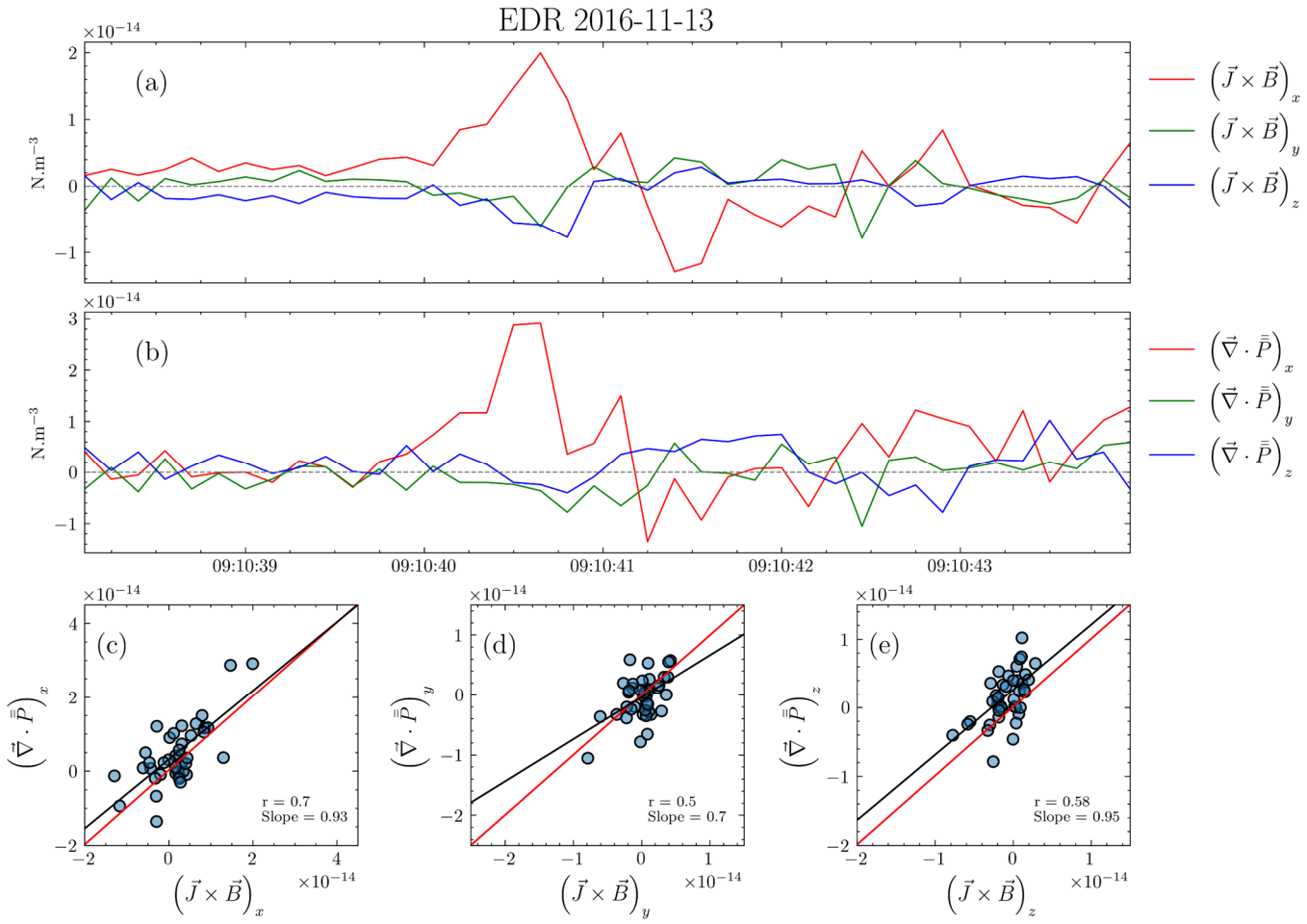

Figure 3: Measurements of $\vec{J}\times\vec{B}$ (panel (a)) and $\vec{\nabla}\cdot\bar{\bar{P}}$ (panel (b)) corresponding to the EDR event in Figure 1. Panels (c)-(e) present scatter plots of $(\vec{J}\times\vec{B})_\alpha$ and $(\vec{\nabla}\cdot\bar{\bar{P}})_\alpha$, with $\alpha = \{x,\ y,\ z\}$, respectively; the black lines represent the linear fit issued from performing a linear regression, and the red lines represent perfect linearity, i.e., slope equals to 1.

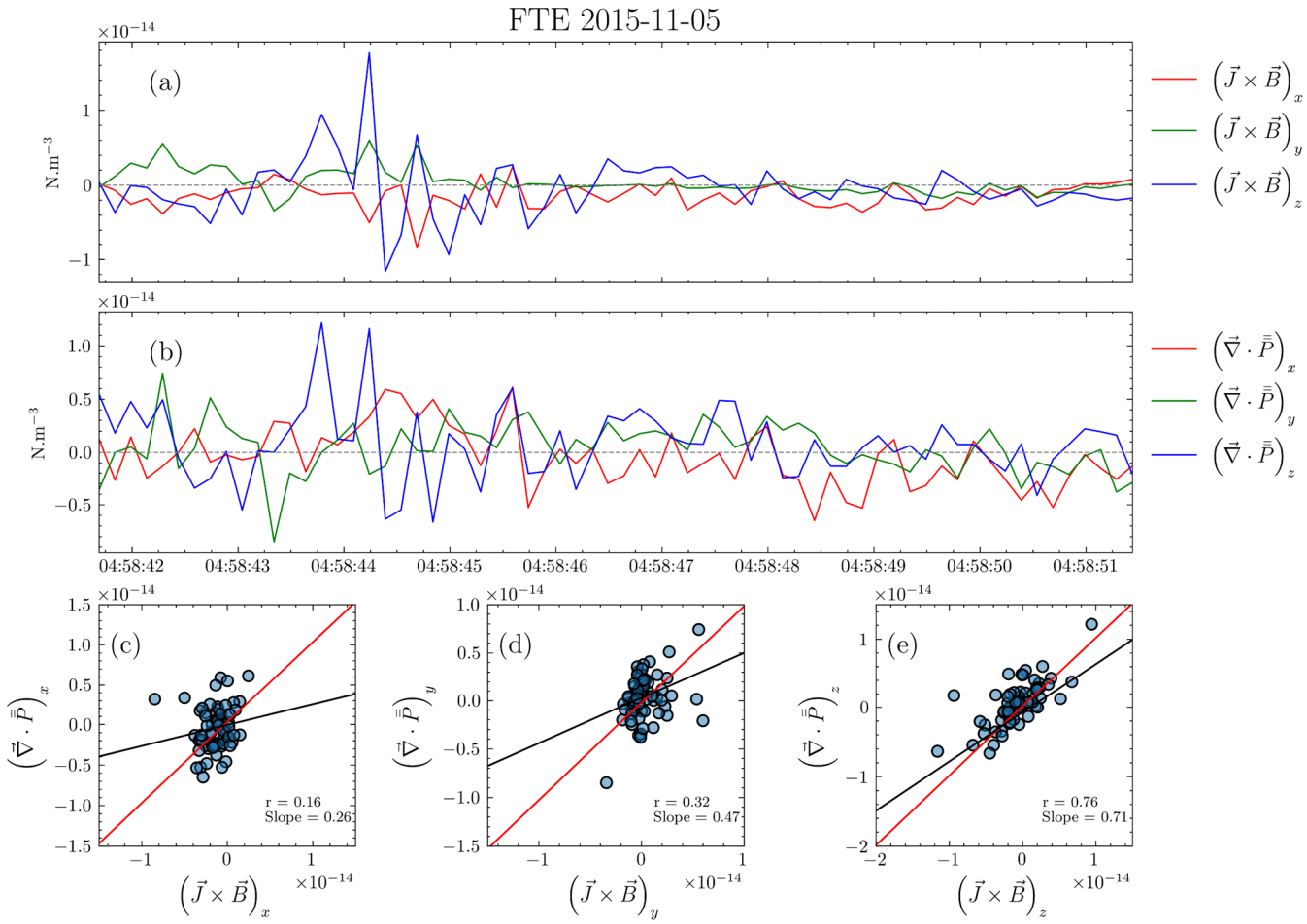

Figure 4: Measurements of $\vec{J}\times\vec{B}$ (panel (a)) and $\vec{\nabla}\cdot\bar{\bar{P}}$ (panel (b)) corresponding to the FTE event in Figure 2. Panels (c)-(e) present scatter plots of $(\vec{J}\times\vec{B})_\alpha$ and $(\vec{\nabla}\cdot\bar{\bar{P}})_\alpha$, with $\alpha = \{x,\ y,\ z\}$, respectively; the black lines represent the linear fit issued from performing a linear regression, and the red lines represent perfect linearity, i.e., slope equals 1.

5.2 Statistical study

Figures 5 and 6 present comprehensive scatter plots illustrating the correlation between $(\vec{J}\times\vec{B})_\alpha$ *and* $(\vec{\nabla}\cdot\bar{\bar{P}})_\alpha$ for every EDR and FTE event in our dataset, respectively. The color-coded bins convey the distribution within each respective bin, offering a visual representation of the distribution. In these scatter plots, the red lines would correspond to perfect force balance, indicating instances where $\vec{J}\times\vec{B} = \vec{\nabla}\cdot\bar{\bar{P}}$. Meanwhile, the black lines correspond to the linear regression fits, revealing the overall alignment between the two terms. To support the results from linear regression fits, we employ an independent method based on binned mean statistics as represented by the green lines. This approach involves averaging $(\vec{\nabla}\cdot\bar{\bar{P}})_\alpha$ for each bin of $(\vec{J}\times\vec{B})_\alpha$. The resulting green lines accurately capture the general trend of the relationship and closely match the fit results. Additionally, the gray shades surrounding the green lines represent the corresponding standard deviations of the binned means.

The EDR scatter plots reveal correlation coefficients along the x, y, and z directions of 0.4, 0.23, and 0.32, respectively. Correspondingly, the slopes for these directions are 0.67, 0.49, and 0.74, respectively. Likewise, the scatter plots for FTEs reveal correlation coefficients of 0.34, 0.29, and 0.4 along the x, y, and z directions, accompanied by slopes of 0.54, 0.52, and 0.54, respectively. Considering the correlation coefficients and the slopes found for both EDRs and FTEs scatter plots, it's evident that there are notable associations along the different directions. To further investigate the statistical significance of these correlations, we examined the associated p-value measures which were found practically zero along the three directions. These results reveal an overall achieved force balance in the monofluid framework along the three directions.

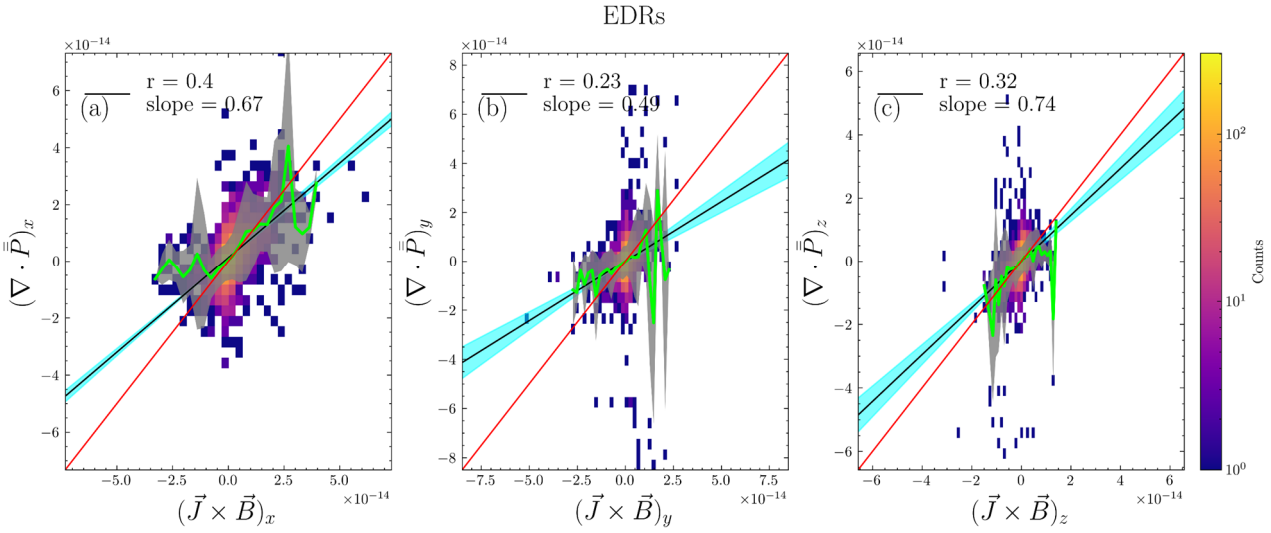

Figure 5: Panels (a)-(c) represents scatter plot histograms of $(\vec{J} \times \vec{B})_\alpha$ *and* $(\vec{\nabla} \cdot \bar{\bar{P}})_\alpha$, with $\alpha = \{x,\ y,\ z\}$, respectively, for every EDR event in our dataset. The black lines represent the linear fit issued from performing a linear regression. The red lines represent perfect linearity, i.e., slope equals 1. The green lines illustrate the binned mean statistics where $(\vec{\nabla} \cdot \bar{\bar{P}})_\alpha$ is averaged for every bin of $(\vec{J} \times \vec{B})_\alpha$. The gray shades illustrate the standard deviation corresponding to the green lines measurements. The blue shades illustrate the standard deviation corresponding to the determination of linear regression's results.

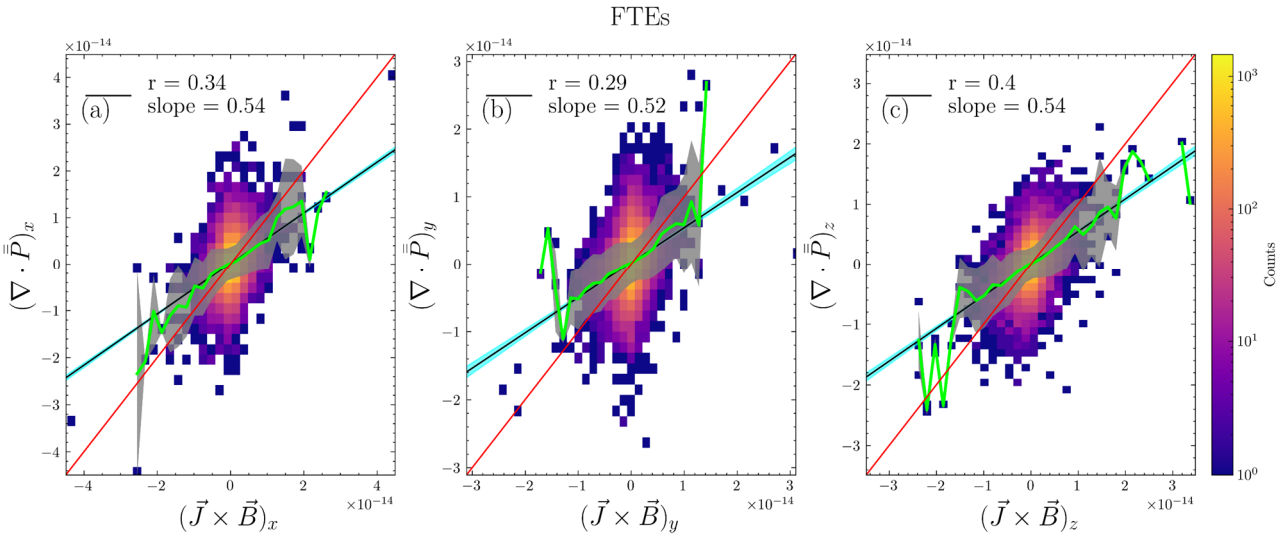

Figure 6: Panels (a)-(c) represents scatter plot histograms of $(\vec{J} \times \vec{B})_\alpha$ *and* $(\vec{\nabla} \cdot \bar{\bar{P}})_\alpha$ *,* with $\alpha = \{x,\ y,\ z\}$, respectively, for every FTE event in our dataset. The black lines represent the linear fit issued from performing a linear regression. The red lines represent perfect linearity, i.e., slope equals 1. The green lines illustrate the binned mean statistics where $(\vec{\nabla} \cdot \bar{\bar{P}})_\alpha$ is averaged for every bin of $(\vec{J} \times \vec{B})_\alpha$. The gray shades illustrate the standard deviation corresponding to the green lines measurements. The blue shades illustrate the standard deviation corresponding to the determination of linear regression's results.

6. Multifluid force balance

We focus in this section on the multifluid terms describing the forces applied on the plasma as introduced in the momentum equation. Similarly to the monofluid framework, the main force terms are the Lorentz force and the pressure gradient force applied to each species. We first analyze two case studies, one for each type of event (EDR and FTE). We then provide statistical results.

6.1. Case studies

Figure 7 presents the measurements of $q_s n_s(\vec{E} + \vec{v}_s \times \vec{B})$ *and* $\vec{\nabla} \cdot \bar{\bar{P}}_s$ for ions and electrons, corresponding to the EDR event introduced in Figure 1, and the relationship between their respective components through scatter plots. We perform linear regressions, represented by the black lines in the scatter plots, while the red lines indicate perfect linearity, i.e., $q_s n_s(\vec{E} + \vec{v}_s \times \vec{B}) = \vec{\nabla} \cdot \bar{\bar{P}}_s$. For each component, we provide the linear correlation measure and the slope resulting from the linear regression.

For electrons, the slopes along the x-, y- and z- directions are 0.33, 0.12 and ~-0.01, respectively. Correspondingly, the correlation coefficients along the x-, y-, z- direction are 0.5, 0.23 and -0.29, respectively. We observe a moderate positive association between the Lorentz force and the pressure gradient force along the x- direction, as indicated by the slope and the correlation coefficient. The relationship is weaker along the y- direction while reversed along the z-direction (negative slope and

correlation coefficient). For ions, the slopes along the x-, y-, z- direction are 0.72, 0.57 and 0.21, respectively. The correlation coefficients along the x-, y- and z- directions are 0.6, 0.48 and 0.3, respectively. The slopes and correlation coefficients are thus much more favorable than for electrons, especially along the x- direction.

Figure 8 presents the same measurements for the FTE event introduced in Figure 2. For electrons, the slopes along the x-, y-, and z- directions are -0.07, 0.06 and -0.02, respectively. The correlation coefficients along the x-, y- and z- directions are -0.16, 0.13 and -0.06, respectively. Unlike the EDR case, the expected balance between the Lorentz force and the pressure gradient force is totally absent along the three directions for electrons. The slopes show that overall, the measurements of electron pressure gradient are significantly smaller than the measured Lorentz force. For ions, the slopes along the x-, y- and z- directions are 0.55, 0.41 and 0.69, respectively. The correlation coefficients along the x-, y- and z- directions are 0.32, 0.32 and 0.80, respectively. Contrary to electrons, ions for this FTE thus show a clear positive, linear relationship between the Lorentz force and the pressure gradient force, especially along the z- direction.

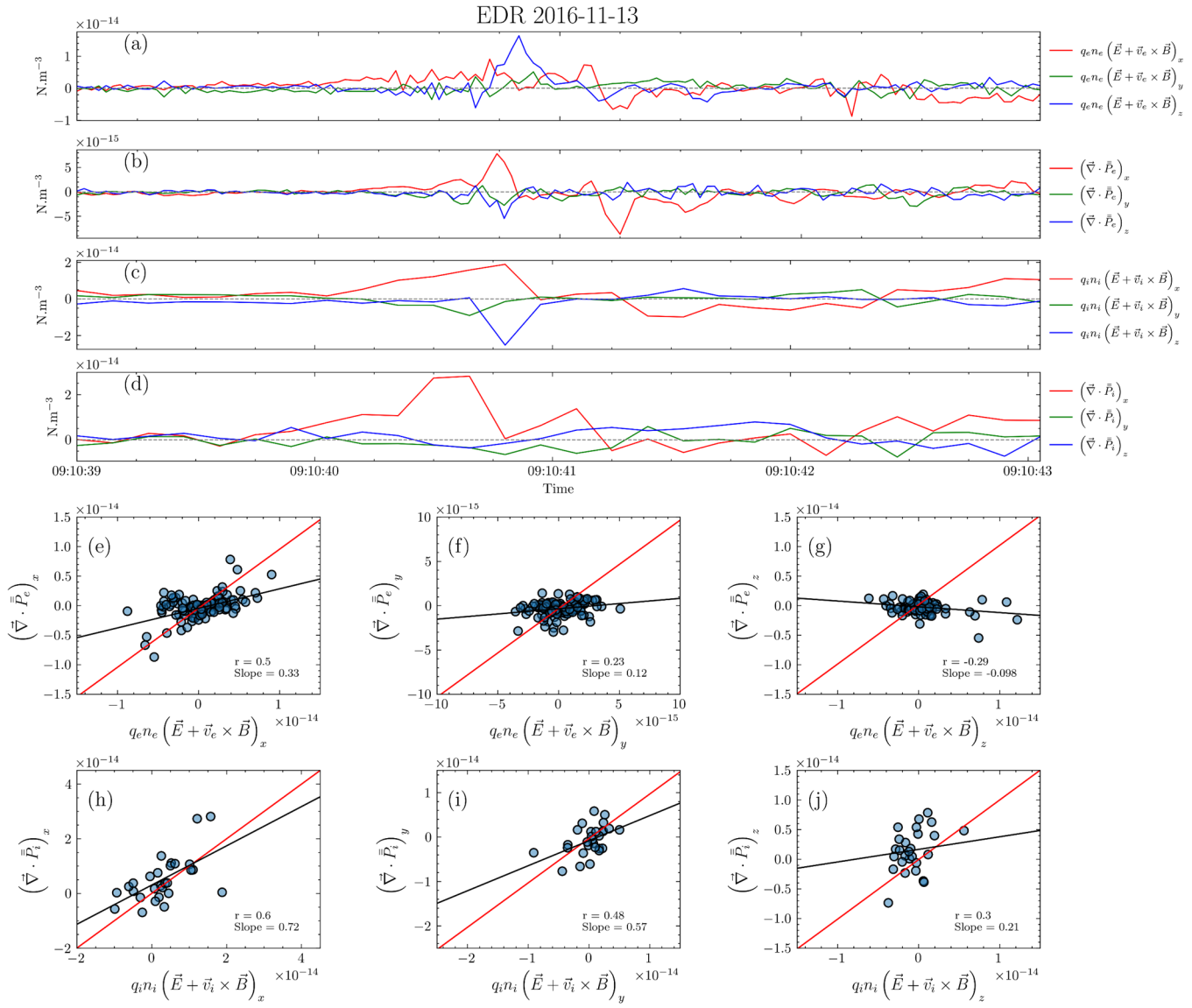

Figure 7: Measurements of $q_s n_s(\vec{E} + \vec{v}_s \times \vec{B})$ and $\vec{\nabla} \cdot \bar{\bar{P}}_s$ corresponding to the EDR event in Figure 1. Panels (a) and (b) present these measurements for electrons, while panels (c) and (d) for ions. Panels (e)-(g) present scatter plots of $(\vec{J} \times \vec{B})_\alpha$ and $(\vec{\nabla} \cdot \bar{\bar{P}})_\alpha$, with $\alpha = \{x,\ y,\ z\}$, respectively, for electrons; panels (h)-(j) for ions. In panels (e)-(j), the black lines represent the linear fit issued from performing a linear regression, and the red lines represent perfect linearity, i.e., slope equals to 1.

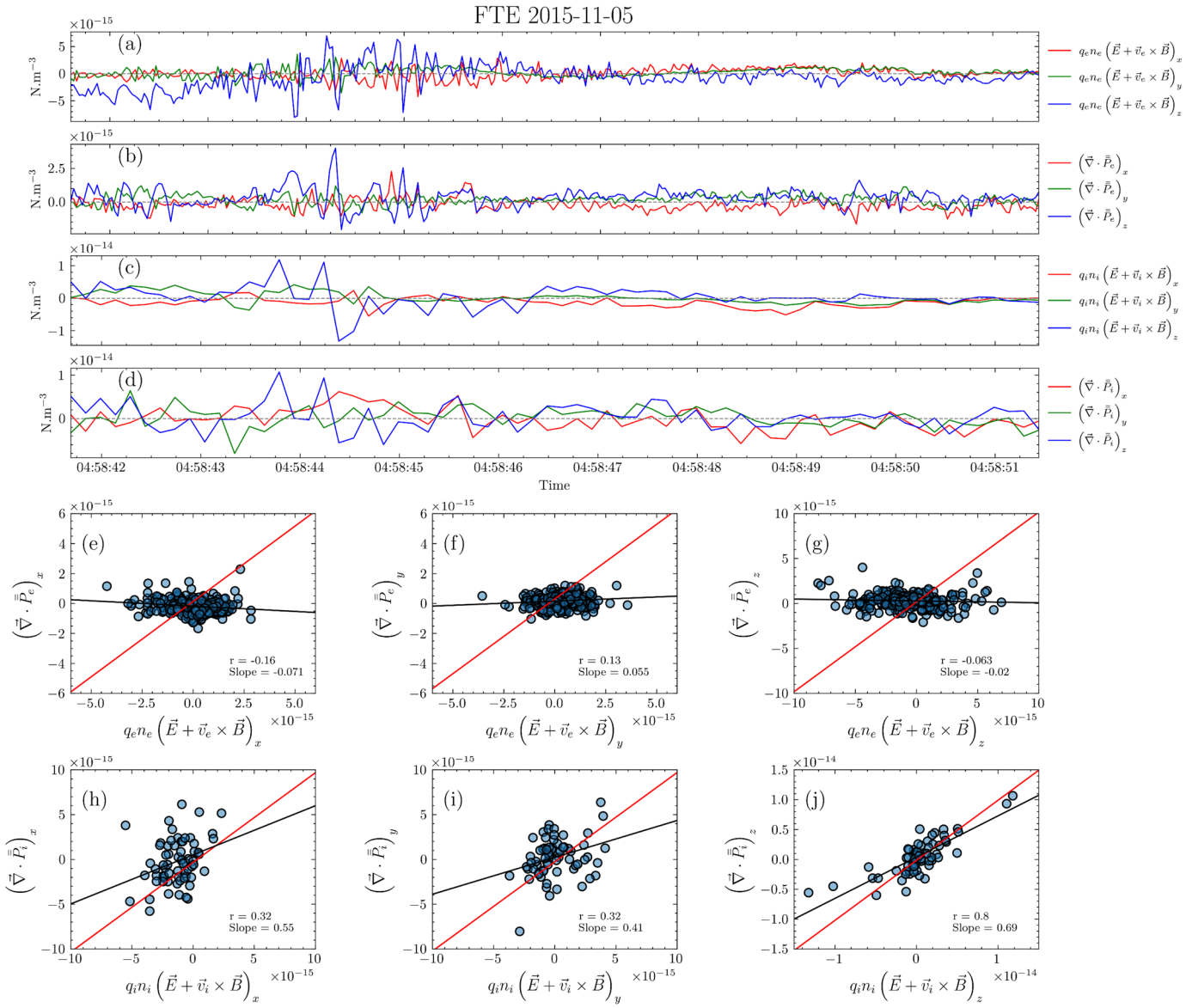

Figure 8: Measurements of $q_s n_s(\vec{E} + \vec{v}_s \times \vec{B})$ and $\vec{\nabla} \cdot \bar{\bar{P}}_s$ corresponding to the FTE event in Figure 2. Panels (a) and (b) present these measurements for electrons, while panels (c) and (d) for ions. Panels (e)-(g) present scatter plots of $(\vec{J} \times \vec{B})_\alpha$ and $(\vec{\nabla} \cdot \bar{\bar{P}})_\alpha$, with $\alpha = \{x,\ y,\ z\}$, respectively, for electrons; panels (h)-(j) for ions. In panels (e)-(j), the black lines represent the linear fit issued from performing a linear regression, and the red lines represent perfect linearity, i.e., slope equals to 1.

6.2. Statistical Study

Figure 9 and 10 present the combined scatter plots illustrating the correlations for electrons and ions between $q_s n_s(\vec{E} + \vec{v}_s \times \vec{B})_\alpha$ *and* $(\vec{\nabla} \cdot \bar{\bar{P}}_s)_\alpha$ for all EDR and FTE events, respectively. The color-coded bins convey the distribution within each respective bin, offering a visual representation of the distribution.

In these scatter plots, the red lines signify perfect force balance, indicating instances where $q_s n_s(\vec{E} + \vec{v}_s \times \vec{B})_\alpha = (\vec{\nabla} \cdot \bar{\bar{P}}_s)_\alpha$. Meanwhile, the black lines correspond to the linear regression fits, revealing the overall alignment between the two terms for electrons and ions. To support the results from

linear regression fits, we employ an independent method based on binned mean statistics as represented by the green lines. This approach involves averaging $(\vec{\nabla} \cdot \bar{\bar{P}}_s)_\alpha$ for each bin of $q_s n_s (\vec{E} + \vec{v}_s \times \vec{B})_\alpha$. The resulting green lines accurately capture the general trend of the relationship and closely match the fit results. Additionally, the gray shades surrounding the green lines represent the corresponding standard deviations of the binned means.

For EDRs, the electron relationship reveals slopes along the x-, y-and z- directions of 0.12, 0.04 and 0.01, and correlation coefficients of 0.14, 0.04 and 0.01, respectively. For ions (panels (d)-(f)), the slopes along the x-, y- and z- directions are 0.96, 0.34 and 0.62, and the correlation coefficients are 0.51, 0.14 and 0.31, respectively. Likewise, for FTEs, the electron (panels (a)-(c)) relationship gives slopes along the x-, y-and z- directions of 0.04, 0.03 and 0.01, and correlation coefficients of 0.12, 0.08 and 0.04, respectively. For ions (panels (d)-(f)), the slopes along the x-, y-and z- directions are 0.48, 0.50 and 0.34, and the correlation coefficients are 0.29, 0.27 and 0.3, respectively. In the same way as the last section, we examined the p-values corresponding to determining the slopes and correlation coefficients. The substantial range of p-values obtained, spanning from the order of $\sim 10^{-17}$ to much lower for ions, reflects the strength and reliability of the observed correlations and slopes (p-value << 0.05). For electrons, however, if we consider that the alternative hypothesis is having positive slopes and correlations, we get notably higher p-values, which is clearly visible from the scatter plots.

These results reveal that the force balance is statistically achieved for measurements of the ion fluid. Electron measurements, however, do not permit to verify the force balance. As shown in the figures, the expected relationship is overall found for ions along the three directions for both EDRs and FTEs. Generally, although much worse for electrons, both ion and electron measurements show pressure gradient significantly smaller than expected for balance with the Lorentz force (slopes smaller than 1).

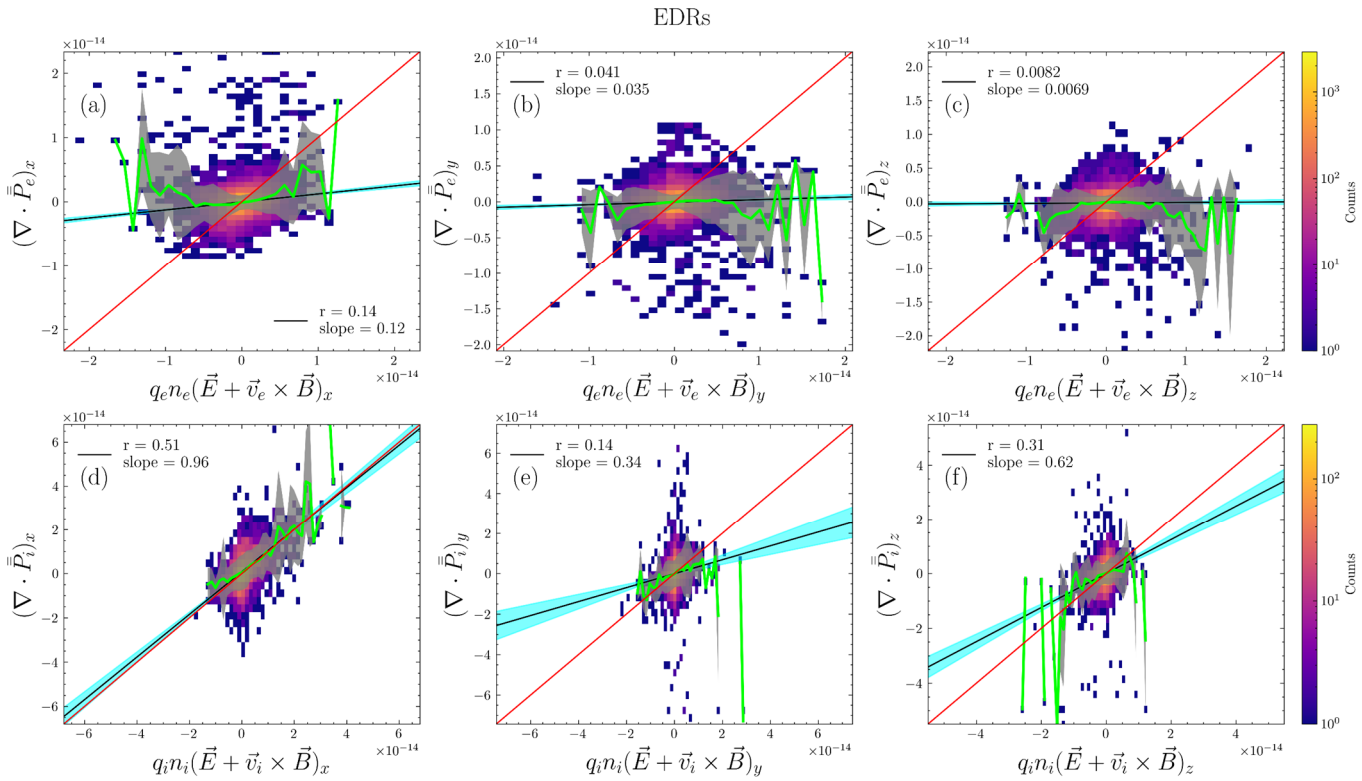

Figure 9: Scatter plot histograms of $q_s n_s(\vec{E} + \vec{v}_s \times \vec{B})_\alpha$ *and* $(\vec{\nabla} \cdot \bar{\bar{P}}_s)_\alpha$, with $s = \{e, i\}$ and $\alpha = \{x,\ y,\ z\}$, for every EDR event in our dataset. Panels (a)-(b) show the relationship for ions for the x-, y- and z- components, respectively for electrons, while panels (d)-(f) for ions. In all the panels, the black lines represent the linear fit issued from performing a linear regression. The red lines represent perfect linearity, i.e., slope equals 1. The green lines illustrate the binned mean statistics where $(\vec{\nabla} \cdot \bar{\bar{P}}_s)_\alpha$ is averaged for every bin of $q_s n_s(\vec{E} + \vec{v}_s \times \vec{B})_\alpha$. The gray shades illustrate the standard deviation corresponding to the green lines measurements. The blue shades illustrate the standard deviation corresponding to the determination of linear regression's results.

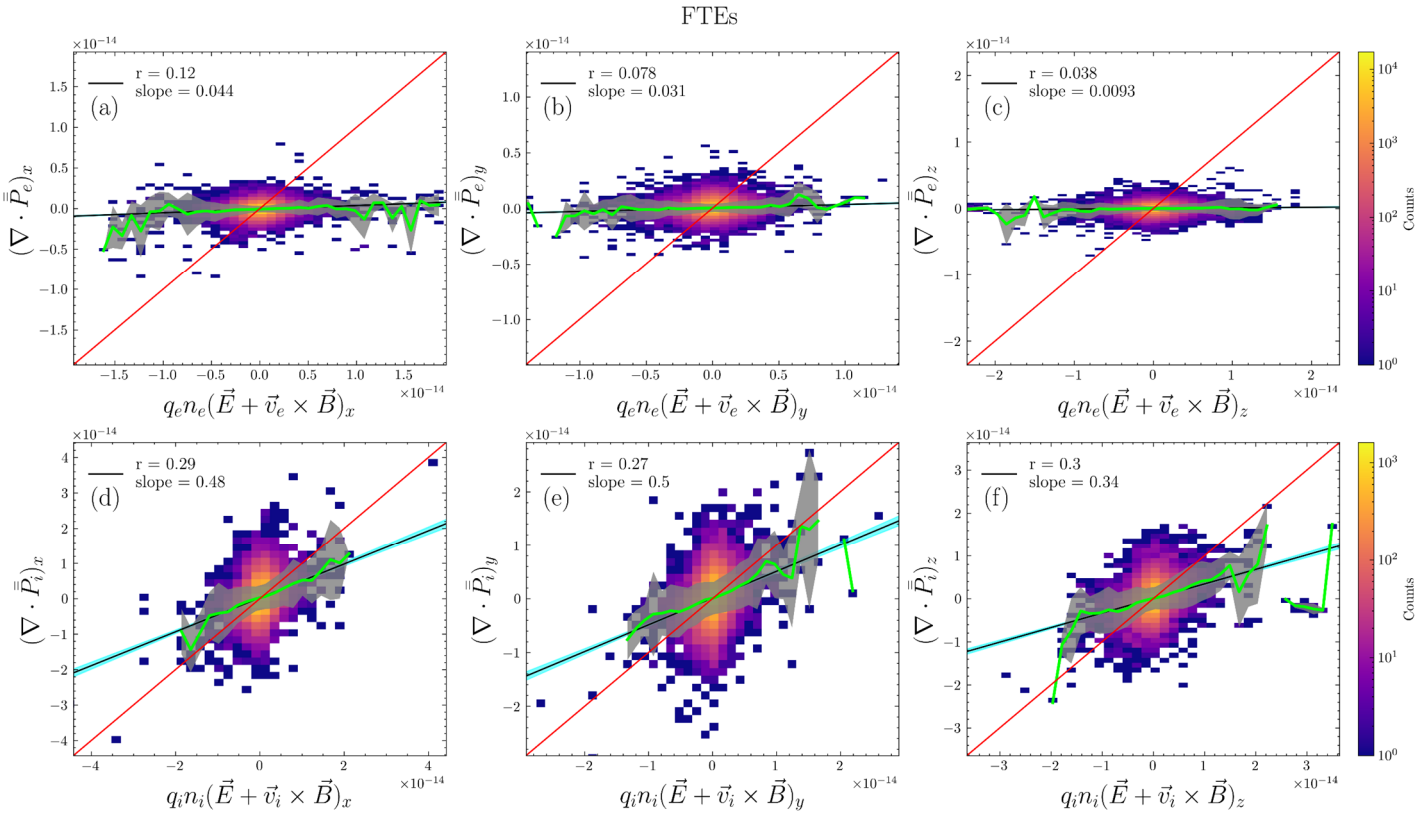

Figure 10: Scatter plot histograms of $q_s n_s(\vec{E} + \vec{v}_s \times \vec{B})_\alpha$ *and* $(\vec{\nabla} \cdot \bar{\bar{P}}_s)_\alpha$, with $s = \{e, i\}$ and $\alpha = \{x,\ y,\ z\}$, for every FTE event in our dataset. Panels (a)-(b) show the relationship for ions for the x-, y- and z- components, respectively for electrons, while panels (d)-(f) for ions. In all the panels, the black lines represent the linear fit issued from performing a linear regression. The red lines represent perfect linearity, i.e., slope equals 1. The green lines illustrate the binned mean statistics where $(\vec{\nabla} \cdot \bar{\bar{P}}_s)_\alpha$ is averaged for every bin of $q_s n_s(\vec{E} + \vec{v}_s \times \vec{B})_\alpha$. The gray shades illustrate the standard deviation corresponding to the green lines measurements. The blue shades illustrate the standard deviation corresponding to the determination of linear regression's results.

7. Multifluid energy balance

We focus in this section on the multifluid terms responsible for changing the kinetic energy density, i.e., $\vec{j}_s \cdot \vec{E}$ *and* $-\vec{v}_s \cdot \vec{\nabla} \cdot \bar{\bar{P}}_s$, as shown in the kinetic energy equation. $\vec{j}_s \cdot \vec{E}$ *and* $-\vec{v}_s \cdot \vec{\nabla} \cdot \bar{\bar{P}}_s$ are responsible for plasma acceleration or deceleration due to electric fields and pressure gradients, respectively. We first analyze two case studies, one for each type of event (EDR and FTE). We then provide statistical results. Unlike the past two sections, here we will keep the minus sign of the pressure gradient term for sake of simplicity in interpreting the terms.

7.1. Case studies

Figure 11 presents the measurements of $\vec{j}_s \cdot \vec{E}$ and $-\vec{v}_s \cdot \vec{\nabla} \cdot \bar{\bar{P}}_s$ for ions and electrons, corresponding to the EDR event introduced in Figure 1. and the relationship between their respective components through

scatter plots. We perform linear regressions, represented by the black lines in the scatter plots, while the red lines indicate perfect linearity, i.e., $\vec{j}_s \cdot \vec{E} = -\vec{v}_s \cdot \vec{\nabla} \cdot \bar{\bar{P}}_s$. For each component, we provide the linear correlation measure and the slope resulting from the linear regression.

Generally, we observe an enhancement (in absolute value sense) around the EDR encounter time in all the terms across panels (a)-(d). We observe a peak in the $\vec{j}_e \cdot \vec{E}$ surpassing the other terms by approximately one order of magnitude. This term is responsible for electron acceleration by transferring magnetic energy to kinetic energy. The magnitude of the peak suggests also that electrons are the main contributors to the Joule dissipation enhancement observed in panel (g). An enhancement in $-\vec{v}_e \cdot \vec{\nabla} \cdot \bar{\bar{P}}_e$ is also observed and approximately collocates with the peak in $\vec{j}_e \cdot \vec{E}$. This suggests that electrons are also being accelerated by the pressure gradient term. By contrast, ions display a negative peak in $\vec{j}_i \cdot \vec{E}$; while they are accelerated by the pressure gradient term.

For electrons, the relationship between $\vec{j}_s \cdot \vec{E}$ *and* $-\vec{v}_s \cdot \vec{\nabla} \cdot \bar{\bar{P}}_s$ is positive, with a correlation coefficient of 0.31. This is unlike what is expected, i.e., negative and linear. Furthermore, the linear regression reveals a slope of 0.06 which indicates that the pressure gradient term is negligible in comparison to $\vec{j}_e \cdot \vec{E}$. However, the ion relationship shows a slope of -0.70 and a correlation coefficient of -0.69. In the ion case, the expected energy balance is thus closely achieved. These findings reflect directly the results obtained in the multifluid force balance.

Figure 12 presents the same measurements for the FTE event introduced in Figure 2. The linear regression for the electrons and ions reveals a slope of 0.01 and -0.71, and a correlation coefficient of 0.09 and -0.78, respectively. As for EDRs, the energy balance in this FTE event is not confirmed from electron measurements The pressure gradient term appears negligible in comparison with $\vec{j}_e \cdot \vec{E}$. Ion measurements, on the other hand, reveal a reasonable energy balance.

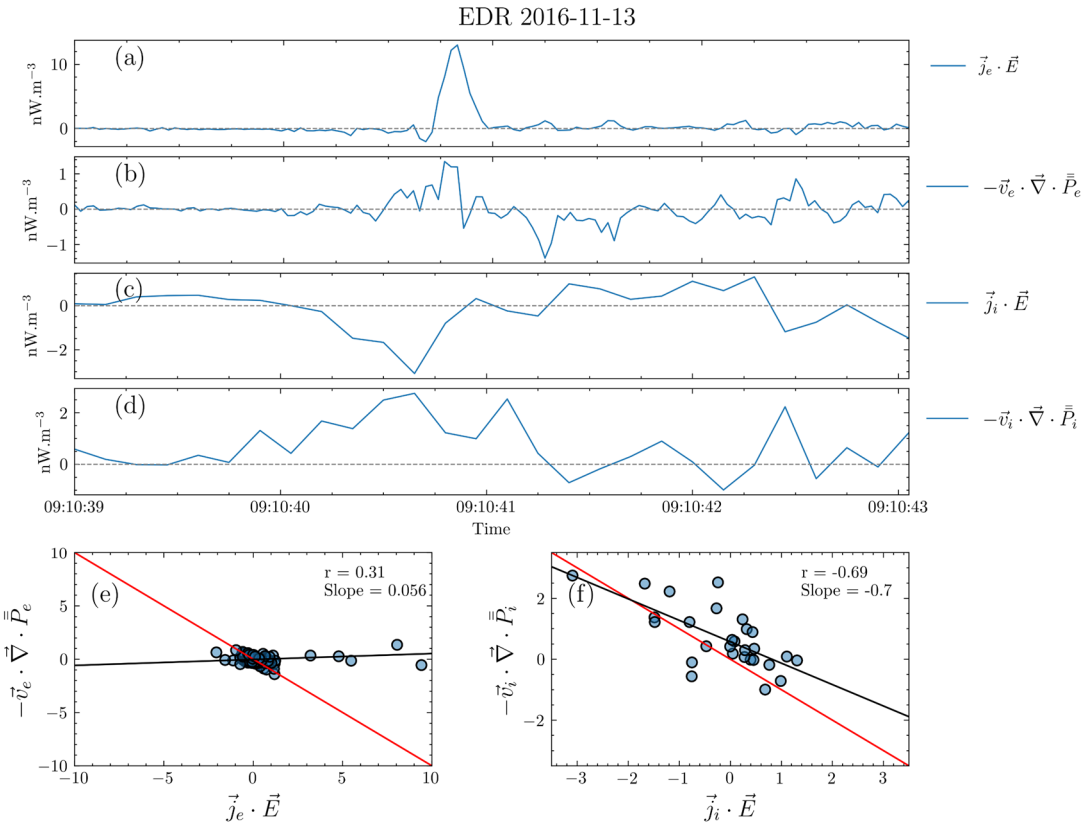

Figure 11: Measurements of $\vec{j}_s \cdot \vec{E}$ and $-\vec{v}_s \cdot \vec{\nabla} \cdot \bar{\bar{P}}_s$ corresponding to the EDR event in Figure 1. Panel (a) and (b) present these measurements for electrons, while panels (c) and (d) for ions. Panel (e) and (f) show scatter plots of $\vec{j}_s \cdot \vec{E}$ and $-\vec{v}_s \cdot \vec{\nabla} \cdot \bar{\bar{P}}_s$ for electrons and ions, respectively. In panels (e) and (f), the black lines represent the linear fit issued from performing a linear regression, and the red lines represent perfect linearity, i.e., slope equals to -1.

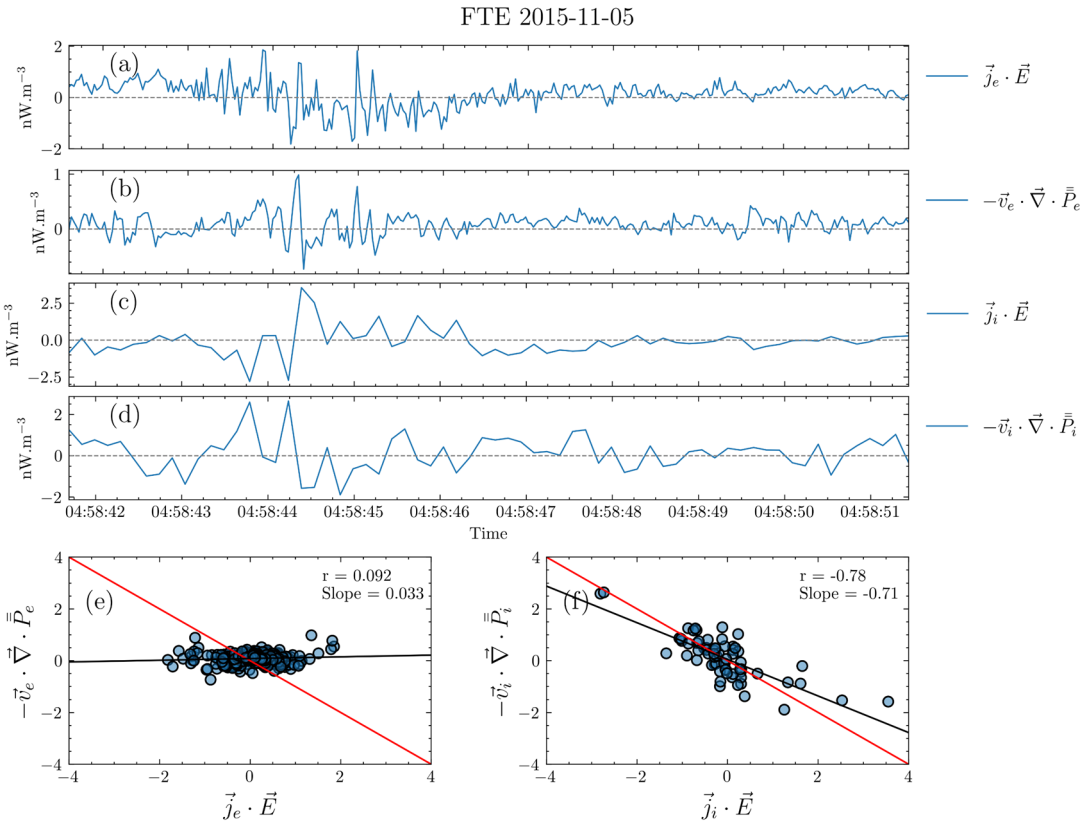

Figure 12: Measurements of $\vec{j}_s \cdot \vec{E}$ and $-\vec{v}_s \cdot \vec{\nabla} \cdot \bar{\bar{P}}_s$ corresponding to the FTE event in Figure 2. Panel (a) and (b) present these measurements for electrons, while panels (c) and (d) for ions. Panel (e) and (f) show scatter plots of $\vec{j}_s \cdot \vec{E}$ and $-\vec{v}_s \cdot \vec{\nabla} \cdot \bar{\bar{P}}_s$ for electrons and ions, respectively. In panels (e) and (f), the black lines represent the linear fit issued from performing a linear regression, and the red lines represent perfect linearity, i.e., slope equals to -1.

7.2. Statistical Study

Figures 13 and 14 present total scatter plots illustrating the correlations for electrons and ions between $\vec{j}_s \cdot \vec{E}$ and $-\vec{v}_s \cdot \vec{\nabla} \cdot \bar{\bar{P}}_s$ for all EDR and FTE events, respectively. The color-coded bins display the distribution within each respective bin, offering a visual representation of the distribution.

In these scatter plots, the red lines signify perfect energy balance, indicating instances where $\vec{j}_s \cdot \vec{E} = -\vec{v}_s \cdot \vec{\nabla} \cdot \bar{\bar{P}}_s$. The black lines correspond to the linear regression fits, revealing the overall alignment between the two terms for electrons and ions. To corroborate the regression fit, we employ an independent method based on a binned mean statistic represented by the green lines. This approach involves averaging $-\vec{v}_s \cdot \vec{\nabla} \cdot \bar{\bar{P}}_s$ for each bin of $\vec{j}_s \cdot \vec{E}$. The resulting green lines accurately capture the general trend of the relationship and closely match the fit results. The gray shades surrounding the green lines represent the corresponding standard deviations for each bin.

For EDRs, the electron relationship reveals that the association between the two terms is weak as suggested from the slope of -0.07 and the correlation coefficient of -0.09. Similarly, the ion relationship reveals statistically a negative overall association between the two terms, however, the expected balance

is more visible than in the electrons. In fact, the linear regression applied to the ion relationship gives a slope of -0.36 and a correlation coefficient of -0.12. Similarly for FTEs, the electron expected linear relationship is absent completely as shown with the slope and correlation coefficient of ~0.01 and 0.03, respectively. In the same way as the last two sections, we examined the p-values corresponding to determining the slopes and correlation coefficients. The ion relationship exhibits negligible p-values, while the electron relationship exhibits important p-values (~ 0.9) under the alternative hypothesis of having negative slope and correlation coefficient.

These results suggest that the expected overall balance between $\vec{j}_s \cdot \vec{E}$ and $-\vec{v}_s \cdot \vec{\nabla} \cdot \bar{\bar{P}}_s$ is statistically observed, although weakly, for ions but it is less clear for electrons. This is clearly different from what was found in the simulations (Fadanelli et al., 2021) where perfect energy balance is exhibited. In the next section we propose some ways to improve the balance by analyzing the sources of errors in the evaluation of the different terms.

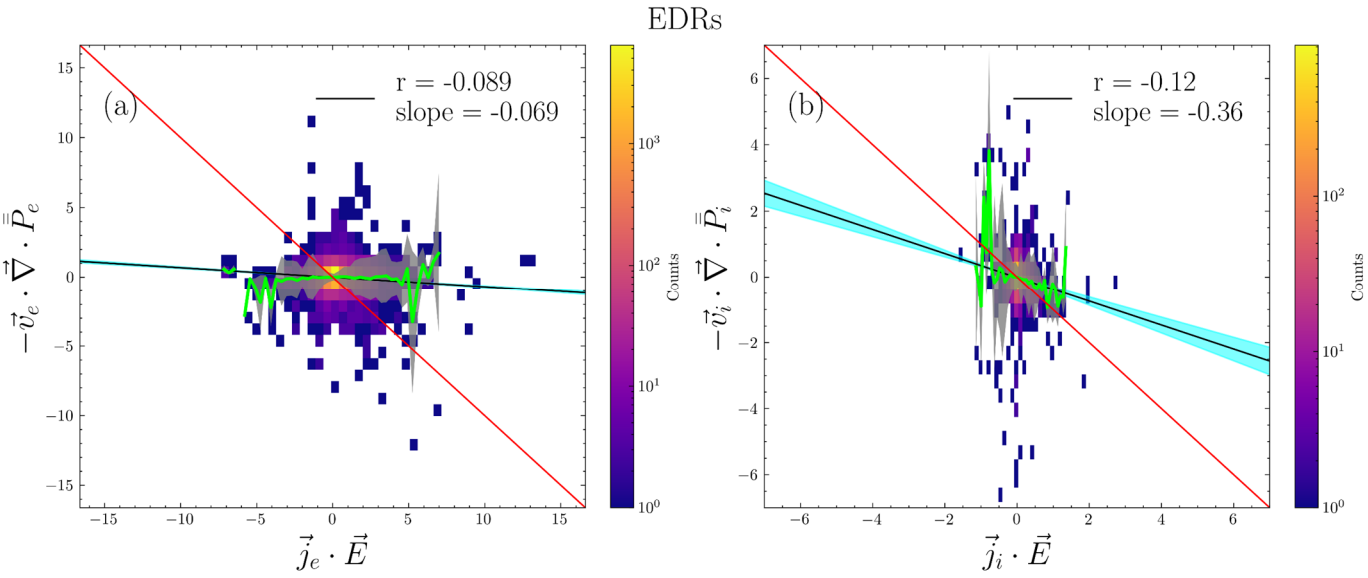

Figure 13: Panels (a) and (b) represents scatter plot histograms of $\vec{j}_s \cdot \vec{E}$ and $-\vec{v}_s \cdot \vec{\nabla} \cdot \bar{\bar{P}}_s$ for electrons and ions respectively, for every EDR event in our dataset. The black lines represent the linear fit issued from performing a linear regression. The red lines represent perfect linearity, i.e., slope equals -1. The green lines illustrate the binned mean statistics where $-\vec{v}_s \cdot \vec{\nabla} \cdot \bar{\bar{P}}_s$ is averaged for every bin of $\vec{j}_s \cdot \vec{E}$. The gray shades illustrate the standard deviation corresponding to the green lines measurements. The blue shades illustrate the standard deviation corresponding to the determination of linear regression's results.

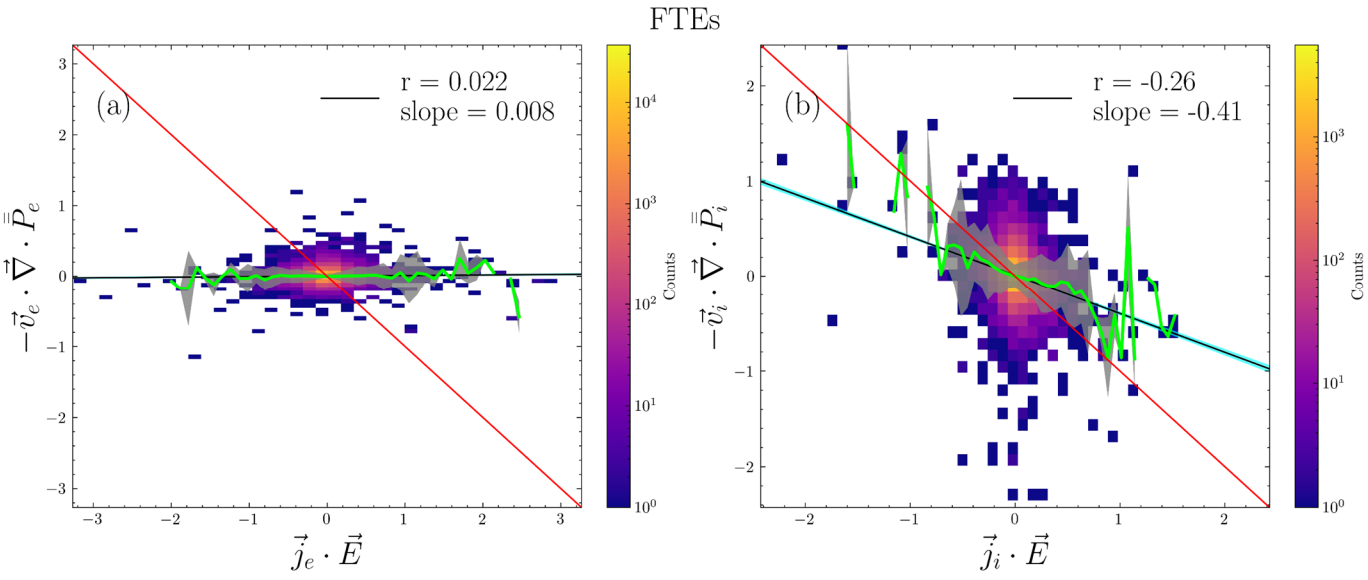

Figure 14: Panels (a) and (b) represents scatter plot histograms of $\vec{j}_s \cdot \vec{E}$ and $-\vec{v}_s \cdot \vec{\nabla} \cdot \bar{\bar{P}}_s$ for electrons and ions respectively, for every EDR event in our dataset. The black lines represent the linear fit issued from performing a linear regression. The red lines represent perfect linearity, i.e., slope equals -1. The green lines illustrate the binned mean statistics where $-\vec{v}_s \cdot \vec{\nabla} \cdot \bar{\bar{P}}_s$ is averaged for every bin of $\vec{j}_s \cdot \vec{E}$. The gray shades illustrate the standard deviation corresponding to the green lines measurements. The blue shades illustrate the standard deviation corresponding to the determination of linear regression's results.

8. Discussion and Conclusions

We studied the balance between the Lorentz force and the pressure gradient force in the monofluid framework, then its extension to the multifluid framework. We also studied the energy balance between the terms responsible for the evolution of the kinetic energy density. These terms are the magnetic energy term ($\vec{j}_s \cdot \vec{E}$) and the pressure gradient term ($-\vec{v}_s \cdot \vec{\nabla} \cdot \bar{\bar{P}}_s$), responsible for plasma acceleration or deceleration with an electric field or a pressure gradient, respectively. We analyzed the balance between these terms in EDRs and FTEs. The monofluid force balance reveals an overall good statistical balance. In the multifluid force balance, we found that balance is statistically achieved only for ion measurements. Electron measurements do not verify the expected force balance. The multifluid energy balance analysis similarly shows an overall energy balance only for the ion fluid, although weaker than for the force balance. Electron measurements again do not exhibit the expected balance. Our monofluid and ion fluid analysis yields notably small p-values (<< 0.01) indicating that the observed correlations between variables, such as the Lorentz force and pressure gradient force, are unlikely to occur purely by chance. Instead, they suggest a meaningful and solid relationship between these parameters. Table 1 summarizes the measured correlations and slopes from the statistical studies. The results obtained through these frameworks remain true for both types of events (EDRs and FTEs), even though they show different statistical correlations. This is expected as the balance between these terms should hold true everywhere

in plasmas regardless of the nature of the event, at least statistically and when the total kinetic energy does not change significantly (relative to each individual source term).

		$(\vec{J} \times \vec{B})_\alpha$ vs $(\vec{\nabla} \cdot \bar{\bar{P}})_\alpha$ (x; y; z)	$q_i n_i (\vec{E} + \vec{v}_i \times \vec{B})_\alpha$ vs $(\vec{\nabla} \cdot \bar{\bar{P}}_i)_\alpha$ (x; y; z)	$q_e n_e (\vec{E} + \vec{v}_e \times \vec{B})_\alpha$ vs $(\vec{\nabla} \cdot \bar{\bar{P}}_e)_\alpha$ (x; y; z)	$\vec{j}_i \cdot \vec{E}$ vs $-\vec{v}_i \cdot \vec{\nabla} \cdot \bar{\bar{P}}_i$	$\vec{j}_e \cdot \vec{E}$ vs $-\vec{v}_e \cdot \vec{\nabla} \cdot \bar{\bar{P}}_e$
EDRs	r values	0.4; 0.23; 0.32	0.51; 0.14; 0.31	0.14; 0.04; 0	-0.12	-0.09
	slopes	0.67; 0.49; 0.74	0.96; 0.34; 0.62	0.12; 0.04; 0	-0.36	-0.07
FTEs	r values	0.34; 0.29; 0.4	0.29; 0.27; 0.3	0.12; 0.08; 0.04	-0.26	0.02
	slopes	0.54; 0.52; 0.54	0.48; 0.5; 0.34	0.04; 0.03; 0	-0.41	0

Table 1: Summary of correlation and slope values from Figures 5, 6, 9, 10, 13 and 14.

While the p-value provides confidence about the slopes and correlation coefficients, we observed that across this analysis, the terms related to the pressure gradient were statistically smaller than their electromagnetic counterpart (slopes < 1). This appears to be strongly the case for the electron relationships in the force and energy balance, in the multifluid framework, where the pressure gradient-related terms are always negligible compared to the electromagnetic terms. The monofluid and ion fluid relationships, although they exhibit a clear correlation between the terms, also suggest that the pressure gradient terms are generally underestimated (see Figures 5, 6, 9, 10, 13 and 14).

We investigated possible errors related to the gradient measurements based on 4-spacecraft technique in order to explain these differences, and to possibly explain the loss of balance in the measurements. Our approach consists in modeling a pressure gradient at a current sheet akin to the magnetopause. We use a current sheet profile of the form $a\ th(x/d) + b$, where a, b and d are the fit parameters. For simplicity we only considered the xx-component of the pressure tensor. The idea is to compare the gradient measurements constructed using a 4-spacecraft technique with the analytical derivative for varying spacecraft separations. We use a regular tetrahedron with a trajectory along the x-direction crossing the pressure gradient in our current sheet profile. The pressure gradient measured from the 4-spacecraft technique is noted $\vec{\nabla}_{4sc} \cdot \bar{\bar{P}}$, while $\vec{\nabla} \cdot \bar{\bar{P}}$ is the regular analytical gradient measure. We quantify the comparison between the constructed gradient and the analytical gradient by comparing their respective maximum value using an error measure as follows:

$$\mathcal{E} = \frac{|(\vec{\nabla}_{4sc} \cdot \bar{\bar{P}})_{x,\,max} - (\vec{\nabla} \cdot \bar{\bar{P}})_{x,\,max}|}{(\vec{\nabla} \cdot \bar{\bar{P}})_{x,\,max}}$$

The black curve in Figure 15 panel (c) summarizes the evolution of this error as measured across a range of the ratio of the spacecraft separation to the local gradient scale. This simple modeling reveals that the error increases as the spacecraft separation gets larger than the gradient scale, such that the constructed gradient is underestimated as the spacecraft separation becomes larger than the gradient scale. This approach is in agreement with Forsyth et al. (2011), who investigated the errors relative to the current measured with the curlometer technique (Dunlop et al., 1988).

In order to project this error analysis into our data, we investigated the distribution of electron (d_e) and ion (d_i) inertial lengths as well as the distribution of MMS separations (determined from the eigenvalues of the volumetric tensor; Paschmann and Dally., 1998) related to our events. Figure 15 panels (a) and (b) show histograms of these quantities for both EDRs (panel (a)) and FTEs (panel (b)). We observe that spacecraft separations are typically larger than electron scales and smaller (or of the same order of magnitude) than the ion scales. Assuming, as a first order approximation, that the characteristic length of the ion (electron) gradient directly scales as the ion (electron) inertial length, the ratio of spacecraft separations to the electron or ion scale helps in understanding the extent of underestimation in our constructed pressure gradient measurements (Figure 15 panel (c)). We observe that ion measurements exhibit errors in the range 10% to 40%, while electron measurements largely exceed 50% error. These findings explain at least part of the statistical results reported in the previous sections, and suggest that caution should be taken in using electron pressure gradient measurements.

We should note that the model used to draw these associations between spacecraft separations and gradient scales is rather simple. In this model, we do not take into account the possible irregularities in the spacecraft tetrahedra nor the measured background noise or other systematic errors (e.g., Vogt et al., 2009; Paschmann and Dally., 1998). Additionally, recently Roberts et al. (2023) discussed errors in the gradient measures that arise from the statistical errors in plasma moments. In particular, they applied this error analysis on the pressure strain term along with its compressible and incompressible decomposition in the context of magnetic reconnection at the magnetopause and the magnetotail. The statistical errors are higher in low density regions (magnetotail) due to poorer instrument count rates. In general, the ion error estimate is higher than that for electrons. Such complementary error analysis will be performed in future work.

These results shed light on the capacity of MMS in capturing the energy and force balance in the monofluid and ion fluid, while they highlight the difficulties encountered in assessing the relationships for the electron fluid. This is notably important in examining and testing Ohm's law terms in which the electric field and electron pressure gradients need to be estimated. While many studies explore the closure of the Ohm's law, it is important to consider possible errors in measuring electron-scale gradients of the pressure tensor.

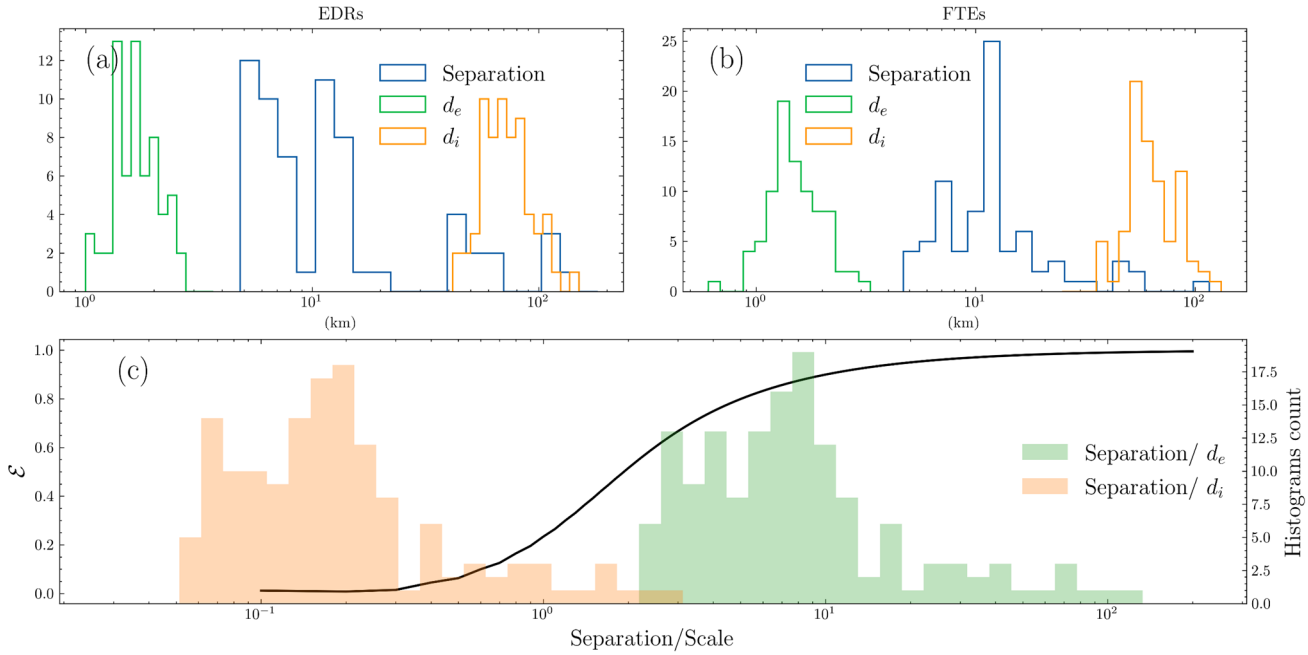

Figure 15: Panels (a) and (b) show distributions of the electron inertial length (d_e; green), the ion inertial length (d_i; orange) and MMS separation (blue) for EDR and FTE events, respectively. Panel (c) shows the error $\mathcal{E}$ (black line; left y-axis) estimated from the modeling described in the discussion, and histograms (right y-axis) of the ratios between the separation and d_e (green) and d_i (orange).

Data Availability Statement

All MMS data are available online at https://lasp.colorado.edu/mms/sdc/public/.

Acknowledgments

We thank the entire MMS team. Work at IRAP was supported by CNRS, CNES and UPS. This study has been partially supported through the grant EUR TESS N°ANR-18-EURE-0018 in the framework of the Programme des Investissements d'Avenir. Our analysis made use of the tools developed at IRAP by the CDPP (AMDA https://amda.irap.omp.eu/, and speasy https://pypi.org/project/speasy/) and E. Penou (CL, https://clweb.irap.omp.eu/). CDPP, the Centre de Donnée de la Physique des Plasmas, is supported by CNRS, CNES, Observatoire de Paris and Université Paul Sabatier, Toulouse.

References

Agudelo Rueda, J. A., Verscharen, D., Wicks, R. T., Owen, C. J., Nicolaou, G., Germaschewski, K., et al. (2022). Energy Transport during 3D Small-scale Reconnection Driven by Anisotropic Plasma Turbulence. *The Astrophysical Journal*, *938*(1), 4. https://doi.org/10.3847/1538-4357/ac8667

Alqeeq, S. W., Le Contel, O., Canu, P., Retinò, A., Chust, T., Mirioni, L., et al. (2022). Investigation of the

homogeneity of energy conversion processes at dipolarization fronts from MMS measurements. *Physics of Plasmas*, *29*(1), 012906. https://doi.org/10.1063/5.0069432

Bandyopadhyay, R., Chasapis, A., Matthaeus, W. H., Parashar, T. N., Haggerty, C. C., Shay, M. A., et al. (2021). Energy dissipation in turbulent reconnection. *Physics of Plasmas*, *28*(11), 112305. https://doi.org/10.1063/5.0071015

Birn, J., & Hesse, M. (2010). Energy release and transfer in guide field reconnection. *Physics of Plasmas*, *17*(1). https://doi.org/10.1063/1.3299388

Burch, J. L., Moore, T. E., Torbert, R. B., & Giles, B. L. (2016). Magnetospheric Multiscale Overview and Science Objectives. *Space Science Reviews*, *199*(1–4), 5–21. https://doi.org/10.1007/s11214-015-0164-9

Burch, J. L., Torbert, R. B., Phan, T. D., Chen, L.-J., Moore, T. E., Ergun, R. E., et al. (n.d.). Electron-scale measurements of magnetic reconnection in space. https://doi.org/10.1126/science

Dunlop, M. W., Southwood, D. J., Glassmeier, K.-H., & Neubauer, F. M. (1988). Analysis of multipoint magnetometer data. *Advances in Space Research*, *8*(9), 273–277. https://doi.org/10.1016/0273-1177(88)90141-X

Eastwood, J. P., Goldman, M. V., Phan, T. D., Stawarz, J. E., Cassak, P. A., Drake, J. F., et al. (2020). Energy Flux Densities near the Electron Dissipation Region in Asymmetric Magnetopause Reconnection. *Physical Review Letters*, *125*(26). https://doi.org/10.1103/PhysRevLett.125.265102

Ergun, R. E., Tucker, S., Westfall, J., Goodrich, K. A., Malaspina, D. M., Summers, D., et al. (2016). The Axial Double Probe and Fields Signal Processing for the MMS Mission. *Space Science Reviews*, *199*(1), 167–188. https://doi.org/10.1007/s11214-014-0115-x

Fadanelli, S., Lavraud, B., Califano, F., Cozzani, G., Finelli, F., & Sisti, M. (2021). Energy Conversions Associated With Magnetic Reconnection. *Journal of Geophysical Research: Space Physics*, *126*(1). https://doi.org/10.1029/2020JA028333

Fargette, N., Lavraud, B., Øieroset, M., Phan, T. D., Toledo-Redondo, S., Kieokaew, R., et al. (2020). On the Ubiquity of Magnetic Reconnection Inside Flux Transfer Event-Like Structures at the Earth's Magnetopause. *Geophysical Research Letters*, *47*(6), 1–9. https://doi.org/10.1029/2019GL086726

Forsyth, C., Lester, M., Fazakerley, A. N., Owen, C. J., & Walsh, A. P. (2011). On the effect of line current width and relative position on the multi-spacecraft curlometer technique. *Planetary and Space Science*, *59*(7), 598–605. https://doi.org/10.1016/j.pss.2009.12.007

Genestreti, K. J., Varsani, A., Burch, J. L., Cassak, P. A., Torbert, R. B., Nakamura, R., et al. (2018). MMS Observation of Asymmetric Reconnection Supported by 3-D Electron Pressure Divergence. *Journal of Geophysical Research: Space Physics*, *123*(3), 1806–1821. https://doi.org/10.1002/2017JA025019

Hasegawa, H., Wang, J., Dunlop, M. W., Pu, Z. Y., Zhang, Q. H., Lavraud, B., et al. (2010). Evidence for a flux transfer event generated by multiple X-line reconnection at the magnetopause. *Geophysical Research Letters*, *37*(16), 1–6. https://doi.org/10.1029/2010GL044219

Khotyaintsev, Yu. V., Graham, D. B., Norgren, C., Eriksson, E., Li, W., Johlander, A., et al. (2016). Electron jet of asymmetric reconnection. *Geophysical Research Letters*, *43*(11), 5571–5580. https://doi.org/10.1002/2016GL069064

Kieokaew, R., Lavraud, B., Fargette, N., Marchaudon, A., Génot, V., Jacquey, C., et al. (2021). Statistical Relationship Between Interplanetary Magnetic Field Conditions and the Helicity Sign of Flux Transfer Event Flux Ropes. *Geophysical Research Letters*, *48*(6), 1–9. https://doi.org/10.1029/2020GL091257

Lenouvel, Q., Génot, V., Garnier, P., Toledo-Redondo, S., Lavraud, B., Aunai, N., et al. (2021). Identification of Electron Diffusion Regions with a Machine Learning Approach on MMS Data at the Earth's Magnetopause. *Earth and Space Science*, *8*(5). https://doi.org/10.1029/2020EA001530

Lenouvel, Quentin. (2022). Identification par apprentissage machine et analyse de régions de diffusion électronique à la magnétopause terrestre observées par la mission MMS, PhD thesis, https://theses.hal.science/tel-04075287v1

Lenouvel, Quentin, Génot, V., & Garnier, P. (2023). List of Electron Diffusion Regions (EDR) observed by NASA/MMS (Version 1) [Data set]. Zenodo. https://doi.org/10.5281/zenodo.8319481

Lindqvist, P.-A., Olsson, G., Torbert, R. B., King, B., Granoff, M., Rau, D., et al. (2016). The Spin-Plane Double Probe Electric Field Instrument for MMS. *Space Science Reviews*, *199*(1), 137–165. https://doi.org/10.1007/s11214-014-0116-9

Norgren, C., Graham, D. B., Khotyaintsev, Yu. V., André, M., Vaivads, A., Chen, L.-J., et al. (2016). Finite gyroradius effects in the electron outflow of asymmetric magnetic reconnection. *Geophysical Research Letters*, *43*(13), 6724–6733. https://doi.org/10.1002/2016GL069205

Øieroset, M., Phan, T. D., Eastwood, J. P., Fujimoto, M., Daughton, W., Shay, M. A., et al. (2011). Direct Evidence for a Three-Dimensional Magnetic Flux Rope Flanked by Two Active Magnetic Reconnection X Lines at Earth's Magnetopause. *Physical Review Letters*, *107*(16), 165007. https://doi.org/10.1103/PhysRevLett.107.165007

Paschmann, G., & Daly, P. (1998). Analysis Methods for Multi-Spacecraft Data. ISSI Scientific Reports Series SR-001, ESA/ISSI, Vol. 1. ISBN 1608-280X, 1998. Retrieved from https://www.semanticscholar.org/paper/Analysis-Methods-for-Multi-Spacecraft-Data.-ISSI-1.-Paschmann-Daly/595da72ae06831683115647b3dfdca84d57e7d1d

Paschmann, G., Haerendel, G., Papamastorakis, I., Sckopke, N., Bame, S. J., Gosling, J. T., & Russell, C. T. (1982). Plasma and magnetic field characteristics of magnetic flux transfer events. *Journal of Geophysical Research: Space Physics*, *87*(A4), 2159–2168. https://doi.org/10.1029/JA087iA04p02159

Pollock, C., Moore, T., Jacques, A., Burch, J., Gliese, U., Saito, Y., et al. (2016). Fast Plasma Investigation for Magnetospheric Multiscale. *Space Science Reviews*, *199*(1–4), 331–406. https://doi.org/10.1007/s11214-016-0245-4

Raeder, J., Flux, J. R., Events, T., & Raeder, J. (2006). Flux Transfer Events : 1 . generation mechanism for strong southward IMF To cite this version : HAL Id : hal-00317942 Annales Geophysicae Flux Transfer Events : 1 . generation mechanism for strong southward IMF.

Rijnbeek, R. P., Cowley, S. W. H., Southwood, D. J., & Russell, C. T. (1982). Observations of reverse polarity flux transfer events at the Earth's dayside magnetopause. *Nature*, *300*(5887), 23–26. https://doi.org/10.1038/300023a0

Roberts, Owen Wyn, Voros, Z., Torkar, K., Stawarz, J. E., Bandyopadhyay, R., Gershman, D. J., et al. (2023). *Estimation of the error in the calculation of the pressure-strain term: Application in the terrestrial magnetosphere. Journal of Geophysical Research: Space Physics, 128, e2023JA031565* https://doi.org/10.1029/2023JA031565

Russell, C. T., & Elphic, R. C. (1978). Initial ISEE magnetometer results: magnetopause observations. *Space Science Reviews*, *22*(6), 681–715. https://doi.org/10.1007/BF00212619

Russell, C. T., Anderson, B. J., Baumjohann, W., Bromund, K. R., Dearborn, D., Fischer, D., et al. (2016). The Magnetospheric Multiscale Magnetometers. *Space Science Reviews*, *199*(1), 189–256. https://doi.org/10.1007/s11214-014-0057-3

Sarto, D. D., & Pegoraro, F. (2018). Shear-induced pressure anisotropization and correlation with fluid vorticity in a low collisionality plasma. *MNRAS*, *475*, 181–192. https://doi.org/10.1093/mnras/stx3083

Shay, M. A., Phan, T. D., Haggerty, C. C., Fujimoto, M., Drake, J. F., Malakit, K., et al. (2016). Kinetic signatures of the region surrounding the X line in asymmetric (magnetopause) reconnection. *Geophysical Research Letters*, *43*(9), 4145–4154. https://doi.org/10.1002/2016GL069034

Slavin, J. A., Imber, S. M., Boardsen, S. A., DiBraccio, G. A., Sundberg, T., Sarantos, M., et al. (2012). MESSENGER observations of a flux-transfer-event shower at Mercury. *Journal of Geophysical Research: Space Physics*, *117*(A12). https://doi.org/10.1029/2012JA017926

Torbert, R. B., Burch, J. L., Giles, B. L., Gershman, D., Pollock, C. J., Dorelli, J., et al. (2016). Estimates of terms in Ohm's law during an encounter with an electron diffusion region. *Geophysical Research Letters*, *43*(12), 5918–5925. https://doi.org/10.1002/2016GL069553

Torbert, R. B., Burch, J. L., Argall, M. R., Alm, L., Farrugia, C. J., Forbes, T. G., et al. (2017). Structure and Dissipation Characteristics of an Electron Diffusion Region Observed by MMS During a Rapid, Normal-Incidence Magnetopause Crossing. *Journal of Geophysical Research: Space Physics*, *122*(12), 11,901-11,916. https://doi.org/10.1002/2017JA024579

Vogt, J., Albert, A., and Marghitu, O.: Analysis of three-spacecraft data using planar reciprocal vectors: methodological framework and spatial gradient estimation, Ann. Geophys., 27, 3249–3273, https://doi.org/10.5194/angeo-27-3249-2009, 2009.

Wang, Y., Bandyopadhyay, R., Chhiber, R., Matthaeus, W. H., Chasapis, A., Yang, Y., et al. (2021). Statistical Survey of Collisionless Dissipation in the Terrestrial Magnetosheath. *Journal of Geophysical Research: Space Physics*, *126*(6). https://doi.org/10.1029/2020JA029000

712 Webster, J. M., Burch, J. L., Reiff, P. H., Daou, A. G., Genestreti, K. J., Graham, D. B., et al. (2018).
713 Magnetospheric Multiscale Dayside Reconnection Electron Diffusion Region Events. *Journal of*
714 *Geophysical Research: Space Physics*, *123*(6), 4858–4878. https://doi.org/10.1029/2018JA025245
715 Yang, Y., Matthaeus, W. H., Parashar, T. N., Haggerty, C. C., Roytershteyn, V., Daughton, W., et al.
716 (2017). Energy transfer, pressure tensor, and heating of kinetic plasma. *Physics of Plasmas*, *24*(7),
717 072306. https://doi.org/10.1063/1.4990421
718 Yao, Z. H., Rae, I. J., Guo, R. L., Fazakerley, A. N., Owen, C. J., Nakamura, R., et al. (2017). A direct
719 examination of the dynamics of dipolarization fronts using MMS. *Journal of Geophysical Research:*
720 *Space Physics*, *122*(4), 4335–4347. https://doi.org/10.1002/2016JA023401
721 Zenitani, S., Hesse, M., Klimas, A., & Kuznetsova, M. (2011). New Measure of the Dissipation Region in
722 Collisionless Magnetic Reconnection. *Physical Review Letters*, *106*(19), 195003.
723 https://doi.org/10.1103/PhysRevLett.106.195003
724 Zhong, Z. H., Deng, X. H., Zhou, M., Ma, W. Q., Tang, R. X., Khotyaintsev, Y. V., et al. (2019). Energy
725 Conversion and Dissipation at Dipolarization Fronts: A Statistical Overview. *Geophysical Research*
726 *Letters*, *46*(22), 12693–12701. https://doi.org/10.1029/2019GL085409
727 Zhou, M., Man, H., Yang, Y., Zhong, Z., & Deng, X. (2021). Measurements of Energy Dissipation in the
728 Electron Diffusion Region. *Geophysical Research Letters*, *48*(24), e2021GL096372.
729 https://doi.org/10.1029/2021GL096372